Tellus
SERIES B
CHEMICAL
AND PHYSICAL
METEOROLOGY
PUBLISHED BY THE INTERNATIONAL METEOROLOGICAL INSTITUTE IN STOCKHOLM

Tellus (2011), 63B, 475–496
Printed in Singapore. All rights reserved

© 2011 The Authors
Tellus B © 2011 John Wiley & Sons A/S

TELLUS

Electron microscopy of particles collected at Praia, Cape Verde, during the Saharan Mineral Dust Experiment: particle chemistry, shape, mixing state and complex refractive index

By K. KANDLER[1]*, K. LIEKE[1], N. BENKER[1], C. EMMEL[2], M. KÜPPER[1], D. MÜLLER-EBERT[1], M. EBERT[1], D. SCHEUVENS[1,2], A. SCHLADITZ[3], L. SCHÜTZ[2] and S. WEINBRUCH[1], [1]*Institut für Angewandte Geowissenschaften, Technische Universität Darmstadt, Schnittspahnstr. 9, 64287 Darmstadt, Germany;* [2]*Institut für Physik der Atmosphäre, Johannes-Gutenberg-Universität, J.-J.-Becherweg 21, 55099 Mainz, Germany;* [3]*Leibniz-Institut für Troposphärenforschung, Permoserstr. 15, 04318 Leipzig, Germany*

(Manuscript received 13 October 2010; in final form 2 May 2011)

ABSTRACT

A large field experiment of the Saharan Mineral Dust Experiment (SAMUM) was performed in Praia, Cape Verde, in January and February 2008. The aerosol at Praia is a superposition of mineral dust, sea-salt, sulphates and soot. Particles smaller than 500 nm are mainly mineral dust, mineral dust–sulphate mixtures, sulphates and soot–sulphate mixtures. Particles larger then 2.5 μm consist of mineral dust, sea-salt and few mineral dust–sulphate mixtures. A transition range exists in between. The major internal mixtures are mineral dust–sulphate and soot–sulphate. Mineral dust–sea-salt mixtures occur occasionally, mineral dust–soot mixtures were not observed. The aspect ratio was 1.3–1.4 for dry particles smaller than 500 nm and 1.6–1.7 for larger ones. Parameterizations are given for dry and humid state. Although the real part of the refractive index showed low variation (1.55–1.58 at 532 nm), a multi-modal imaginary part was detected as function of particle size, reflecting the complex composition. Soot mainly influences the absorption for wavelengths longer than the haematite absorption edge, whereas for shorter wavelengths dust is dominating. The refractive index of the aerosol depends on the source region of the mineral dust and on the presence/absence of a marine component.

1. Introduction

Mineral dust is one of the major constituents of the atmospheric aerosol. By its influence on the radiation field it impacts the earth's climate (Carlson and Benjamin, 1980; Tegen, 2003; Satheesh and Krishna Moorthy, 2005; Mahowald et al., 2006). A major uncertainty in the mineral dust radiative impact lies in the poor description of particle composition and particle shape (Durant et al., 2009). A coating on top of the mineral dust particles is able to change the radiative impact (Bauer et al., 2007), and the mixing state can significantly alter the optical properties of the particles (Nousiainen, 2009; Redmond et al., 2010). In addition, mineral dust influences cloud microphysics with regard to the liquid and to the ice phase (DeMott et al., 2003; Andreae and Rosenfeld, 2008; Zimmermann et al., 2008; Min et al., 2009). The mineral dust composition itself and the reactivity of the particles influence the cloud droplet activation properties (Kelly et al., 2007; Sullivan et al., 2009). An addition of small amounts of soluble material mixed with mineral dust can change activation significantly (Gibson et al., 2007). Finally, after its deposition onto the planetary surface mineral dust impacts ecosystems by supplying locally unavailable trace substances (Swap et al., 1992; Jickells et al., 2005; Koren et al., 2006) or adversely, by transporting microorganisms and pollutants (Shinn et al., 2000; Garrison et al., 2003; Garrison et al., 2006).

During the Saharan Mineral Dust Experiment (SAMUM) field campaigns (Heintzenberg, 2009; Ansmann et al., 2011),

*Corresponding author.
Institut für Angewandte Geowissenschaften, Technische Universität Darmstadt, Schnittspahnstr. 9, 64287 Darmstadt, Germany.
e-mail: kzk@gmx.de
DOI: 10.1111/j.1600-0889.2011.00550.x

comprehensive microphysical, chemical and optical properties of mineral dust—fresh as well as transported—and its admixtures like sea-salt and biomass burning aerosol as well as gas phase-derived constituents (i.e. ammonium sulphate) were investigated. Although the primary objective of SAMUM was assessing the direct radiative impact of mineral dust aerosol, a large data set was obtained from which also implications for cloud processing or ecosystem impact can be derived.

In this paper, results of off-line aerosol measurements at the SAMUM ground station at Praia, Cape Verde, are presented. The aerosol composition, state of mixture, refractive indices and particle shape are investigated by electron-microscopical single particle analysis, which provides a unique tool to assess the chemical and mineralogical composition of each particle together with information on the particle shape and its volatility. Although automated scanning electron microscopy enables investigation of thousands of particles, manual measurement by scanning and transmission electron microscopy (TEM) yields a very detailed knowledge about a smaller number of particles regarding their internal structure, mixing state and mineralogical composition. The combination of both methods in conjunction with a detailed aerosol characterization by online measurements yields detailed insights into the relevant mineral dust properties. Consequently, electron microscopy was used during several recent experiments in and around the Sahara (e.g. Falkovich et al., 2001; Blanco et al., 2003; Hoornaert et al., 2003; Reid et al., 2003a,b; Alastuey et al., 2005; Petit et al., 2005; Moreno et al., 2006; Kandler et al., 2007; Chou et al., 2008; Formenti et al., 2008; Coz et al., 2009; Kandler et al., 2009; Twohy et al., 2009; Matsuki et al., 2010).

2. Methods

The SAMUM ground station during the SAMUM-2 experiment in 2008 was located on the airport of Praia, Cape Verde, at 14°56'50.89″N and 23°29'4.31″W, approximately 110 m a.s.l. Particle collection was performed on top of an aerosol measurement container. All instruments were adjusted to a sampling altitude of 4 m above ground. The container was placed at the northeast corner of the Praia station area to minimize local contamination. For details refer to Kandler et al. (2011).

Three major dust events have been recorded: DU1 from 17 to 20 January, DU2 from 24 to 26 January and DU3 from 28 January to 2 February, separated by transitional periods. At the beginning and at the end of the campaign there were maritime periods (MAR1, MAR2). In the following, the combination of DU1, DU2 and DU3 is denoted as 'dust situation' and that of MAR1 and MAR2 as 'maritime situation'. For details on the meteorology, microphysical properties and bulk mineralogical composition of the periods refer to Kandler et al. (2011) and Knippertz et al. (2011).

The SAMUM ground station during the SAMUM-1 experiment in 2006 was located 35 km southeast of the city of Zagora in southern Morocco on the Drâa river flood plains, at the edge of the highly arid Saharan desert areas (30°14'15″N, 5°36'29″W, approximately 680 m a.s.l.). The same measurement container was deployed in Morocco as described. For details refer to Kandler et al. (2009).

2.1. Sampling and analysis

Aerosol particles were collected with cascade impactors, a free-wing impactor and a sedimentation trap. Single-nozzle miniature cascade impactors were mounted on a three-dimensional wind vane for iso-axial sampling to minimize inlet losses of large particles (Kandler et al., 2007; Kandler, 2009). Four impactor stages were used with nominal 50% efficiency cut-offs at 2.5 μm, 1 μm, 500 nm and 100 nm approximately. Particles larger than 1 μm were collected on pure carbon adhesive, smaller particles on TEM grids (Plano TEM grids S-162 N3, Wetzlar, Germany). A free-wing impactor (Jaenicke and Junge, 1967; Kandler et al., 2009) was used to collect particles larger than approximately 10 μm on pure carbon adhesive on copper plates. A Sigma-2 sampler (VDI, 1997) was used as sedimentation trap, collecting particles between 3 and 50 μm, approximately, on pure carbon adhesive mounted on 25 mm aluminium electron microscopy stubs. All samples were stored and transported under dry conditions (silica gel) to avoid modification due to high humidity.

A total of 242 sample substrates for electron microscopy were collected in 101 separate aerosol samplings. Depending on the particle size range and aerosol concentration, the sampling times varied between 5 sec and 10 min. The different samplers were run in parallel to achieve a representative concurrent sampling of all particle size ranges. If that was not possible due to technical reasons, the time interval between the sampling periods was kept as short as possible. In Table 1, an overview of the sampling times and the according meteorological situations are given.

About 48,500 individual particles were analysed with a scanning electron microscope (SEM: FEI ESEM Quanta 200 FEG, Eindhoven, The Netherlands). The samples were analysed under vacuum condition (approx. 10^{-2} Pa) without any preparation. The samples were screened for distinctive features possibly constricting the use of the automated particle analysis, for example unusual high concentrations of commonly rare elements, unusual particles shapes or deposition patterns indicating possible artefacts or local contamination, very high or very low particle concentrations, traces of liquids, etc. After successful screening (94% of the samples were fully usable), the samples were analysed automatically by the software-controlled electron microscope (software EDAX/AMETEK GENESIS 5.231). The automated analysis was performed on the carbon adhesive with the backscatter electron signal, and on TEM grids with the secondary electron signal. An acceleration voltage of 20 kV, 'spot size 4' (lateral beam extension 2.6 nm) and a working distance of approximately 10 mm were used for all samples analysed automatically. Appropriate magnifications were chosen for the

Table 1. Sampling times and meteorological periods during the SAMUM-2 campaign in winter 2008 at Praia, Cape Verde.

Date	Time	Period
13 Jan	15:50–16:52	MAR1
14 Jan	18:59–19:00	MAR1
15 Jan	16:43–16:44	MAR1
15 Jan	18:33–18:43	MAR1
16 Jan	10:30–10:40	MAR1
16 Jan	16:52–17:51	MAR1
17 Jan	11:20–11:30	T
18 Jan	10:09–10:19	DU1
18 Jan	15:39–15:54	DU1
19 Jan	10:16–10:26	DU1
19 Jan	18:18–18:28	DU1
21 Jan	16:22–16:38	T
22 Jan	12:06–12:16	T
22 Jan	15:43–15:53	T
23 Jan	13:36–14:18	T
23 Jan	17:23–17:33	T
24 Jan	11:06–11:21	DU2
25 Jan	10:49–10:59	DU2
25 Jan	15:03–15:13	DU2
27 Jan	10:19–10:51	T
28 Jan	09:13–09:26	T
28 Jan	16:50–17:04	DU3
29 Jan	11:37–11:48	DU3
29 Jan	19:23–19:33	DU3
30 Jan	15:53–16:03	DU3
30 Jan	19:17–19:27	DU3
31 Jan	10:41–10:51	DU3
01 Feb	10:06–10:48	DU3
02 Feb	10:15–10:33	DU3
03 Feb	10:11–10:21	T
04 Feb	15:03–15:13	T
04 Feb	18:03–18:15	MAR2
05 Feb	13:52–14:02	MAR2
05 Feb	17:26–18:11	MAR2
06 Feb	13:24–13:34	MAR2
07 Feb	10:15–10:25	MAR2
08 Feb	10:25–10:36	MAR2
09 Feb	10:02–10:12	MAR2
10 Feb	09:55–10:05	MAR2

DU, mineral dust period; MAR, maritime period; T, transition period.

different particle size regimes: 590 nm pixel^{-1} for particles larger than 3 μm diameter, 74 nm pixel^{-1} for larger than 1 μm, 37 nm pixel^{-1} for larger than 300 nm, 13–17 nm pixel^{-1} for smaller than 500 nm diameter.

Assuming a random orientation of the particles, the size of each particle is calculated as the equivalent projected area diameter d:

$$d = \sqrt{\pi^{-1} 4B} \tag{1}$$

with B the area covered by the particle.

The volume of the particles was calculated assuming random particle orientation as

$$V = \frac{\pi}{6} d^3. \tag{2}$$

The chemical composition of the particles (all elements with $Z \geq 6$) was determined by energy-dispersive X-ray microanalysis with an Si (Li) detector. X-ray count rates were corrected for matrix effects using the so-called 'standardless' procedures provided by the Ametek Genesis software, but not for particle shape effects. The concentration of C, N, O, Cu and Ni in the particles cannot be determined accurately due to a contribution of the sampling substrates or weak signals. As a result, nitrogen compounds and organic matter could not be investigated quantitatively. For particles with diameters larger than 500 nm, the classification of the particles into chemical classes was performed according to the scheme shown in Table S1. For smaller particles, the signal-to-noise ratio is low during automated analysis, so especially the discrimination of soot, sulphate and quartz is not reliable. Thus, the classification of these particles was performed manually for selected samples, taking into account the X-ray spectrum, morphological features and the characteristic alteration under electron bombardment. The resulting number abundance ratios for soot, sulphate and quartz from the manual classification was then scaled to the number of particles not clearly identified by their chemical composition automatically (i.e. all particles except halogenides, non-quartz silicates, silicate sulphate mixtures, carbonates and iron oxides; refer to Table S1).

An element index is introduced for visualization. This index is defined as the atomic ratio of the concentration of the element considered and the sum of the concentrations of the elements Na, Mg, Al, Si, P, S, Cl, K, Ca, Ti, Cr, Mn and Fe. The elements C, N, O, Cu and Ni were not included in the calculation of the element index. The element index in this work will be symbolized by vertical bars, for example as |Si|.

TEM was performed with a Philips CM 20 (Philips, Eindhoven, The Netherlands) operated at 200 kV accelerating voltage and a LaB_6 gun. TEM images were recorded with a high-resolution CCD camera (KeenView G2, Olympus Soft Imaging Solutions GmbH, Münster, Germany) mounted at the bottom of the transmission electron microscope. The Transmission electron microscope is coupled to an energy-dispersive X-ray microanalysis with an Si (Li) detector.

2.2. *Particle mixing state*

The particle mixing state was assessed by a three component model. Si, S and Cl were used as tracer elements for

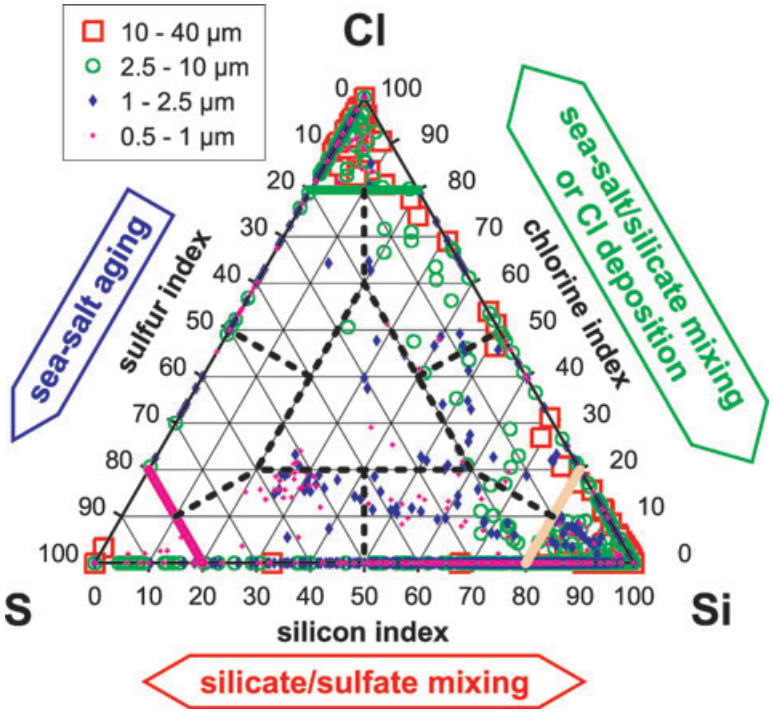

Fig. 1. Three component mixing model for a dust situation (DU3) at Praia, Cape Verde, for particles with $|Si+S+Cl| > 0.4$. The model scheme for mixtures of silicate mineral dust, sulphate and sea-salt is shown as arrows depicting the most probable particle modification process. Particle diameter classes are shown by different symbols. The division between "pure" regions (corners), binary mixture regions (edges) and the ternary mixture region (centre) is shown by thick lines.

the assumed main components, silicate, sulphate and sea salt. Figure 1 shows the main mixing axes of the three components indicated by these tracers as large arrows. Pre-requisite for this approach is that the particles are dominantly composed of these elements. A criterion of $|Si+S+Cl| > 0.4$ was used for discrimination: 70% of the particle number and 85% of the particle volume—which was calculated from the particle number size distribution of the particles investigated in SEM—fulfilled this prerequisite. Particles not assessed by this scheme were mainly Ca- and Fe-rich as well as Al-dominated silicates. The resulting ternary distributions were split into three 'pure' regions, six binary regions, where one compound dominates over the other, and a ternary mixing region. Although the element index is not an exact quantification of elemental contents—particles size and shape effects (Armstrong, 1991; Ro et al., 2003; Laskin et al., 2006) could not be regarded in this work—it is a systematic tool for mixing state discrimination. Figure 1 gives an example of the ternary mixture for the dust period DU3 at Praia (for description of the meteorological periods refer to Kandler et al., 2011; Knippertz et al., 2011). Particles were counted for each region and classified by their size. The mean of each mixing type for each size class was determined as average volume-weighted abundance.

To address in general the significance of a measurement of the mixing state by an off-line single particle analysis method, the coincidence error has to be estimated, that is the chance that a newly depositing particle touches another particle, so that the particles cannot be discriminated by their shape and internal mixing is detected as an artefact. The easiest model of coincidence error determination is done by estimating the chance of touching for a newly impacting, infinitely small particle. This chance equals the area fraction covered by the already deposited particles. The mean area coverage fraction for all samples was 0.025. With the assumption that the area coverage increases linearly from zero at the beginning of the particle collection to the mean area coverage, the average coverage over the sampling time—and, thus, the coincidence error—is half of that value, 0.013. Assuming homogeneous impaction behaviour, the sum of the relative abundances of all mixture groups must be greater than this value to be significant. This significance was achieved for most days in the sub-micrometre range, for approximately half of the days in the diameter range between 1 and 2.5 µm, and for a few days only for the particles larger than 2.5 µm.

For particles smaller than 500 nm diameter, the automatically measured chemical information exhibits a too high uncertainty to apply the chemical ternary mixing. In addition, soot plays an important role in this size range, which is not included in the chemical mixing model. Thus, a manual investigation of mixing state was performed by TEM analysis. Randomly selected particle ensembles were imaged. Afterwards, the selected area was extensively irradiated by the electron beam to remove volatile material. Finally, the same area was imaged again, and the difference in area for each particle between the two images was measured (software ImageJ; Rasband, 2010). The refractory/non-refractory volume was estimated from the areas to the power of 1.5. Because of the extremely high time requirement of this type of work, only two samples could be investigated, one from the maritime period and one from the dust period.

2.3. Refractive index determination

To determine the complex refractive index of the individual particles, the measured chemical composition has to be simplified because (a) the mineralogical phase could not be determined for each particle in this work and (b) the spectral optical base properties for the identifiable components are not available in each case. The composition is modelled by nine pure compounds, for which spectrally resolved refractive indices are available. Where no value for refractive index is available at the required wavelength in literature, a linear interpolation between the adjacent wavelengths was performed. As shown by Kandler et al. (2011), kaolinite is one of the main silicate components in the aerosol at Cape Verde. Because no refractive index data for the additionally identified feldspar components are available, the silicate component has to be replaced by kaolinite only. The kaolinite refractive index data are taken from Sokolik and Toon (Sokolik and Toon, 1999). However, as the real part of the refractive index given by the authors does not match with other available databases (e.g., Anthony et al., 2003; see also Nousiainen, 2009), only the spectral dependency from Sokolik and Toon (1999) is used, and the values are shifted to 1.56 at 550 nm wavelength. All sulphate components are modelled by pure ammonium sulphate (Ivlev and Popova, 1972), as again no more spectral optical properties for the other sulphate components are available. For the following materials, literature data were used unmodified: haematite (Sokolik and Toon, 1999), rutile (Ribarski, 1985), quartz (Philipp, 1985), calcite (Tropf, 1998), sodium chloride (Eldridge and Palik, 1985) and potassium chloride (Palik, 1985). The complex refractive index of soot was taken from the flame soot measurements of Chang and Charalampopoulos (1990), which were shown to represent the optical properties of atmospheric soot in the Atlantic ocean region (Bergstrom et al., 2002).

Depending on the classification of each particle, the model composition of the particle was determined by calculating volume fractions of the pure components from tracer elements and specific densities for each compound. Table S1 gives the model compounds for each particle group as well as the tracer elements used for calculation. Note that the presence of the haematite model compound is checked for most of the soil particle groups, as most of the mineral dust particles contain at least traces of iron. With the same reasoning as for Morocco (Kandler et al., 2009), only one fourth of the total iron content is assumed to be present as haematite. From these volume fractions, by application of a volume mixture rule (Ouimette and Flagan, 1982)—that is assuming completely homogeneous internal mixture—the spectral complex refractive index for each particle is calculated.

The main sources of uncertainty for this approach are systematic: the occurrence of iron in oxides and in silicates, the quality of the available base data for pure minerals, the exact mineral phase determination and the determination of the soot content. Smaller uncertainties arise from quantification errors of the chemical composition and statistical counting errors. We use the large range reported in the literature for the iron oxide/total iron ratio (see also Kandler et al., 2009) as an estimate for the uncertainty of the refractive index in the mineral dust size regime and in addition for the particles smaller than 500 nm a counting error of the rare pure soot particles, which contribute significantly to the total soot volume. The total uncertainty of the imaginary part is estimated as a factor of 2 for particles larger than 500 nm and a factor of 3 for smaller ones. Assuming a low variation in the systematic uncertainties, the relative precision (i.e. for the relative difference between the single measurements) is higher than the given factors: 30% relative in the imaginary part for particles larger than 500 nm and a factor of 2 for the smaller particles. The overall uncertainty for the real part of the refractive index is much lower; an average uncertainty of 0.03 (absolute) is estimated.

2.4. Particle shape

The shape of the dry particles is derived from image analysis in the SEM. There are several available shape descriptors, of which the two-dimensional aspect ratio (AR) is chosen, because it is least sensitive to image artefacts and least depending on image resolution (Podczeck et al., 1999; Almeida-Prieto et al., 2007). The aspect ratio is calculated as

$$\mathrm{AR} = \frac{\pi L^2}{4B} \tag{3}$$

with L is the longest projection of the particle outline and B is the area covered by the particle.

The aspect ratio expresses the particle elongation, for example by this definition a circle has AR = 1, a chicken egg cross-section AR = 1.28–1.42 (spot test derived from 20 images), a rectangle twice as long as wide AR = 1.96, two adhering circles AR = 2 and a rectangle three times as long as wide AR = 2.62. The aspect ratio was determined for each particle. From this data set, size-dependent aspect ratio density distributions were derived. These distributions are parameterized by a modified log-normal distribution, which yields functions describing the original discrete distributions with high accuracy (Kandler et al., 2007).

The investigation of particles in an electron microscope under vacuum conditions implies measurement under dry conditions, so common soluble materials are effloresced. At Cape Verde, in contrast, high relative humidities can occur. As the aerosol contains significant fractions of soluble material, the according particles then are expected to be in solution and, thus, possess a spherical shape rather than the effloresced shape determined in the electron microscope. Figure 2 shows an estimate for the solution state of three major aerosol components during the campaign. Two cases are considered as limits for the estimate. In the dry limiting case, shown in black, it is assumed that the relative humidity measurements at the station are representative

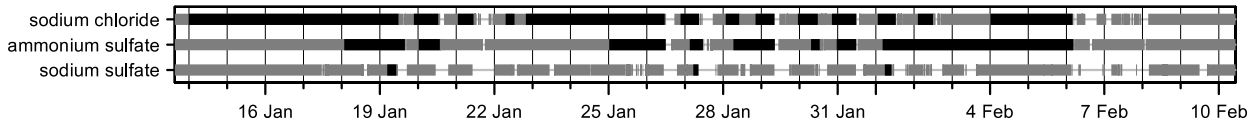

Fig. 2. Potential deliquescence states for sodium chloride (NaCl), ammonium sulphate ($(NH_4)_2SO_4$) and sodium sulphate (Na_2SO_4) derived from the relative humidity measurements at the Praia ground station (Kandler et al., 2011). The deliquescence and efflorescence relative humidities were taken from Martin (2000). A thick line shows the periods where these salts would be deliquesced: black line—all according particles are deliquesced; grey line—particles having experienced high relative humidities before are still deliquesced.

for the particle history, and all collected particles undergo deliquescence and efflorescence. In the wet limiting case, shown in grey, it is assumed that due to the measurement location on an island, all particles have experienced high relative humidities before and arrive in deliquesced state. However, Fig. 2 shows that neither case is representative for the whole campaign, so a total deliquesced as well as a total effloresced case will be discussed. To estimate the shape in the deliquesced case, all particle classes containing soluble compounds (refer to Table S1; classes: secondary, sulphates and chlorides; groups: all mixtures with sulphate or sodium chloride) were assumed to be spherical. The size of each soluble particle was assumed to increase by the size-dependant average measured growth factor at 85% relative humidity (Schladitz et al., 2011). For each size class, the fraction of spherical particles is determined, and the aspect ratio density distribution is determined for the non-spherical fraction only as described.

3. Results and discussion

3.1. Particle composition

During the measurement campaign at Praia in 2008, three major dust events were recorded: DU1 from 17 to 20 January, DU2 from 24 to 26 January and DU3 from 28 January to 2 February, of which DU2 and DU3 had very similar source characteristics. For details on the meteorology of the periods, refer to Knippertz et al. (2011) and Kandler et al. (2011). These intensive dust periods were separated by transitional periods with a mixture of local and marine influence together with mineral dust. Starting from 3 February, mineral dust concentrations decrease, and a maritime period (MAR2) is observed. In addition, before the first dust event another maritime period occurred (MAR1). Note that 'maritime' refers to the meteorological transport pattern and absence of particular dust emission in the source regions, but not necessarily describes the aerosol composition literally.

The classification in terms of composition shows differences between the dust and the maritime periods, but no significant variation between the separate dust periods or within them. Therefore, averages of the dust periods (DU1, DU2, DU3) and the maritime periods (MAR1, MAR2) were calculated and are addressed as 'dust period' and 'maritime period', respectively. Figure 3 shows these averages for the dust and maritime period at Praia. Within each size class shown in the diagram, the particles were weighted according to their volume in view of the volume weighting for the refractive index calculation below. It is apparent, that the composition is a function of particle size in a similar manner for both aerosol types. Silicate particles have the largest abundance in the super micrometre size range. During the dust events, they contribute about 30–50% also to the submicrometre range, whereas this contribution is lower (15–30%)

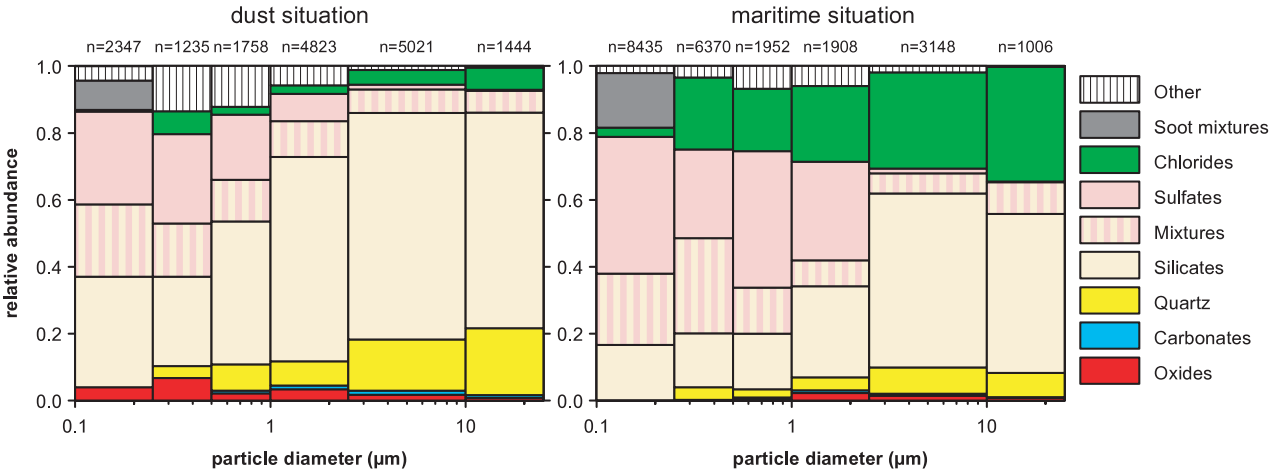

Fig. 3. Size-resolved volume-averaged composition of the aerosol at Praia, Cape Verde, in 2008. Above the diagram, the number of particles analyzed in each size class is shown. See text for details.

during the maritime situation. There is always a small amount of quartz particles present in an approximately constant ratio to the amount of silicates. However, during the dust situation there is a tendency of higher quartz abundances towards larger particles, which was already found—much more pronounced—for Tinfou, Morocco (Kandler et al., 2009). In the size range smaller than 1 μm there is always a significant fraction of sulphate. In the maritime case, also many particles between 1 and 2.5 μm diameter are sulphates. A more detailed analysis (shown in Schladitz et al., 2011, Fig. 11) reveals that these super micrometre sulphate particles consist of sodium sulphate, whereas the ones smaller than 500 nm consist mainly of ammonium sulphate. In between, a transition regime exists. Within the smallest size class, soot particles and soot sulphate mixtures were identified in significant number. Their abundance is higher in the maritime situation than during the dust periods. The major difference between dust and maritime situations is of course the contribution of sodium chloride. Although there is less than 10% sodium chloride abundance in the super micrometre range during the dust periods, its contribution raises to an average of 30% during the maritime situations. A maximum abundance of 80% was reached during the maritime periods, which exhibited in general a higher variability than the dust periods. In any case, mineral dust at Cape Verde plays a significant role even during maritime meteorological situations when no particular dust plume is advected, which confirms results at Sal measured decades ago (Jaenicke and Schütz, 1978). Another difference between the dust and maritime situations is reflected in the abundance of iron-rich particles (oxides), which is higher in the submicron range during the dust situation, although no significant difference is present in the super micrometre range. Finally, the overall contribution of calcium-dominated particles (carbonates) is negligible, which is in large contrast to the measurements in Tinfou, Morocco (Kandler et al., 2009). This difference can be explained by the chemical composition of the soils in the different source regions for Morocco and Cape Verde (e.g. Claquin et al., 1999).

Mineralogical bulk analysis has shown (Kandler et al., 2011) that at least four mineral phases are present in the aerosol at Praia, which are classified as silicate by the single particle analysis: plagioclase, K-feldspar, kaolinite and illite. To assess a potential change in silicate composition, all measured particles larger than 500 nm classified as silicate are plotted in Fig. 4, which shows a comparison of the chemical fingerprint for Praia, dust and maritime situations, and Morocco. In Figs 4a–c, the (Mg+Fe)/Si ratio (*x*-axis), Al/Si ratio (*y*-axis) and the (Na+K+Ca)/Si ratio (*z*-axis, colour-coded) for each single particle are shown. In addition, Figs 4d–i show the relative number abundance of the silicate particles as function of the mentioned elemental ratios by colour. These mineral 'tracer ratios' were chosen because (a) the Al/Si ratio as the signal of the two main components exhibits the least uncertainty and varies significantly for different mineral phases, which are shown in addition in Fig. 4; (b) The (Mg+Fe)/Si ratio is an indicator for clay mineral aggregates, as feldspars are commonly poor in these elements (Anthony et al., 2003; Barthelmy, 2010); (c) in contrast, the (Na+K+Ca)/Si ratio would be significantly higher for feldspars than for clay minerals.

First, three main clusters are visible in Figs 4a–c. Close to and in the graph origin there is a cluster of highly Si-dominated particles, which are most probably quartz particles with small impurities (cluster 1). Secondly, at around (Mg+Fe)/Si = 0.05, Al/Si = 0.4 and (Na+K+Ca)/Si = 0.25 there is a small cluster (2). These particles are mainly rich in K (not shown as separate graph), so this cluster can be addressed as the (K-)feldspars identified by X-ray diffraction (Kandler et al., 2011). Third, there is a widely spread cluster (3) incorporating most of the particles with a modal centre at about (Mg+Fe)/Si = 0.2–0.3, Al/Si = 0.5–0.6 and (Na+K+Ca)/Si = 0–0.1. In contrast to the feldspar cluster, where the pure mineral phases are close to the centre, no unique elemental fingerprint of a single mineral can be attributed to this cluster. It can be concluded—in accordance with the day-by-day electron-microscopical observations—that most of the silicate particles are present as aggregates of inhomogeneous mineralogical composition. In addition, detailed observation has shown (Kandler et al., 2009; Lieke et al., 2011; Scheuvens et al., 2011) that these aggregates may incorporate—besides different silicates—optical active substances like iron oxides or titanium oxides. Although the position of the feldspar cluster is the same for all shown situations, the aggregate cluster shows a shift of the modal centre along the (Mg+Fe)/Si axis from 0.2 (Praia dust situation) to 0.3 (Praia maritime and Tinfou, Morocco). Presently, there is no obvious explanation for this behaviour. The extension of the aggregate cluster at Tinfou towards high values of (Na+K+Ca)/Si ratio with low number abundances is attributed to a mixture of silicate aggregates with sodium sulphate (reanalysis of the data of Kandler et al., 2009), which were not detected in significant abundances at Praia. Otherwise, the relative abundances of the three clusters in the silicate fraction of the total aerosol are remarkably similar for all situations.

In contrast, if the composition of the silicate particles is considered as function of particle size, a clear change in composition is visible. Figure 5 shows the size-dependence of the mineral tracer ratios abundances at Praia. Most of the silicates in the submicron size range have nearly no contribution of Mg, Fe, Na, K or Ca. Although it cannot be totally excluded, that small amounts of these elements are overlooked due to the low signal-to-noise ratio for the small particles, particles of this size are less probably aggregates than larger ones, as they are in the same size range as primary clay grains. Particles between 1 and 2.5 μm in diameter show a higher contribution especially of Mg+Fe, indicating a more complex aggregate structure than the smaller ones, including probably iron oxides. At these particle sizes, pure feldspar minerals do not occur. Between 2.5 and 10 μm most of the particles have contributions of Mg+Fe, which is in accordance with the observation of aggregate dominance for this size range. In this size range, a minor amount of pure (in contrast to aggregated) particles is present. Finally, for the largest

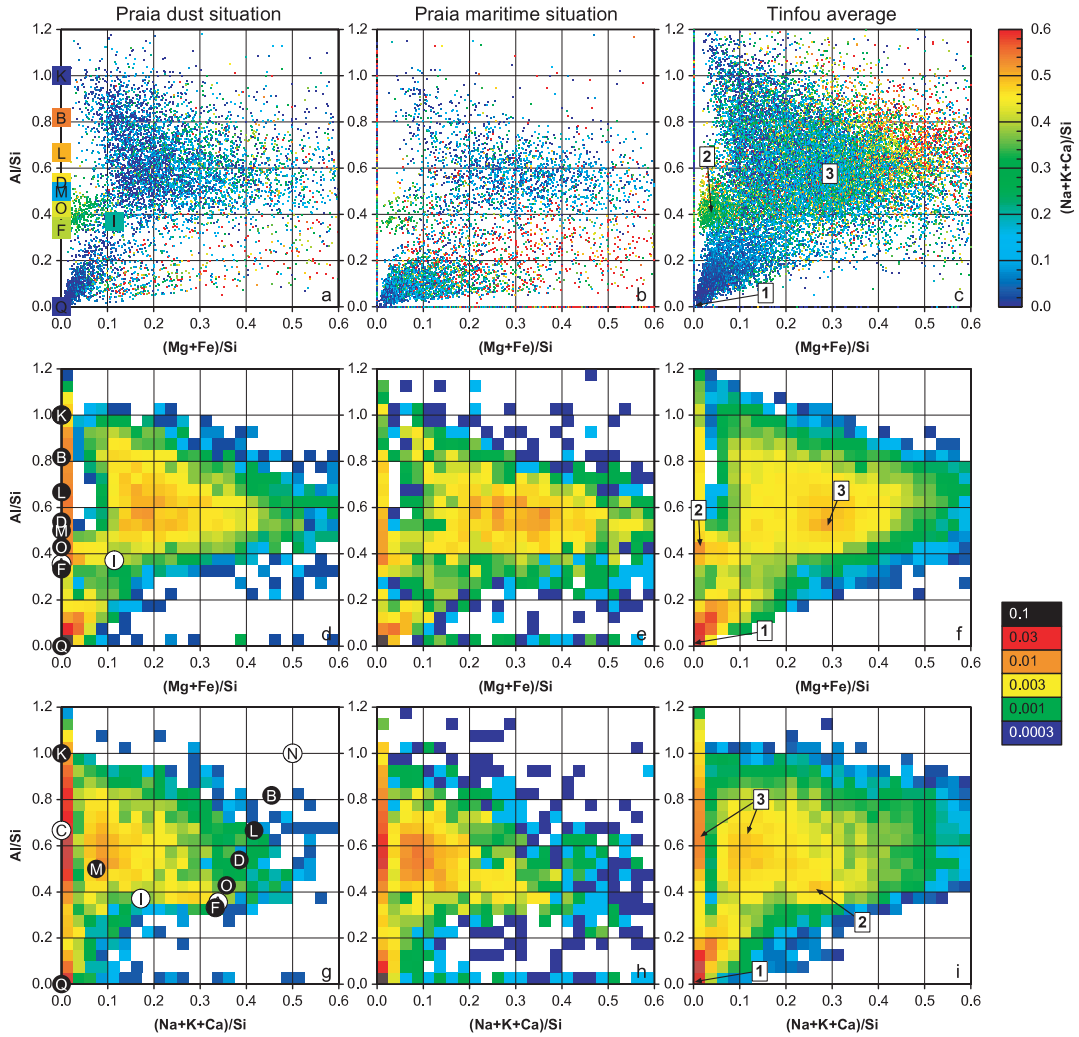

Fig. 4. Comparison of silicate particle composition for dust and maritime situations and for Morocco. The upper row (a–c) shows scatter plots for all silicate and quartz particles larger than 500 nm. The two lower rows (d–i) show fraction distributions of frequency of occurrence normalized with respect to the total number of silicate particles. The gap in the lower plots between ratio 0.025 and 0.05 is an inevitable artefact caused by the EDS quantification algorithm. The position of pure mineral components is shown by lettered symbols: (Q) quartz, (K) kaolinite, (I) illite, (C) chlorite: clinochlore, (K) K-feldspar, (A) albite, (O) plagioclase: oligoclase, (D) plagioclase: andesine, (L) plagioclase: labradorite, (B) plagioclase: bytownite, (N) anorthite, (M) montmorillonite, (T) biotite. Black symbols indicate, that the presence of the mineral phases was shown by X-ray diffraction (Kandler et al., 2011), in case of plagioclase for the mineral group only. Exemplary, in the Tinfou graphs c, f and i, the three main clusters are marked by numbers: (1) quartz cluster, (2) feldspar cluster, (3) clay mineral/aggregate cluster.

particles feldspars contribute to a significant fraction. In addition, the quartz cluster shows a higher abundance than for smaller particles, consistently with the compositional classification.

Iron is one of the most important compounds of mineral dust with respect to atmospheric processes (radiation transfer, ice nucleation, input of nutrients into ecosystems). It can be present in particles as different species (e.g. Lázaro et al., 2008). Iron can be incorporated into the crystal structure of clay minerals where it does not influence optical properties significantly (Karickhoff and Bailey, 1973). In addition, it can be present as iron oxides such as haematite, goethite and magnetite, which exist as separate iron-rich particles as well as small grains in silicates (Kandler et al., 2009; Scheuvens et al., 2011). In the latter case, these grains can be distributed throughout the aggregate volume or, less frequent, reside on the surface for more compact particles, which was shown by detailed analysis of single particles (Scheuvens et al., 2011). To assess the iron distribution on basis of many particles in a quantitative way, Fig. 6 shows the size-resolved abundance of particles classified with respect to their iron content. Four main particle types are shown in this graph: (a) silicates with low iron content ($|\mathrm{Fe}| < 0.1$), (b) particles with high iron contents ($|\mathrm{Fe}| > 0.1$), (c) silicates

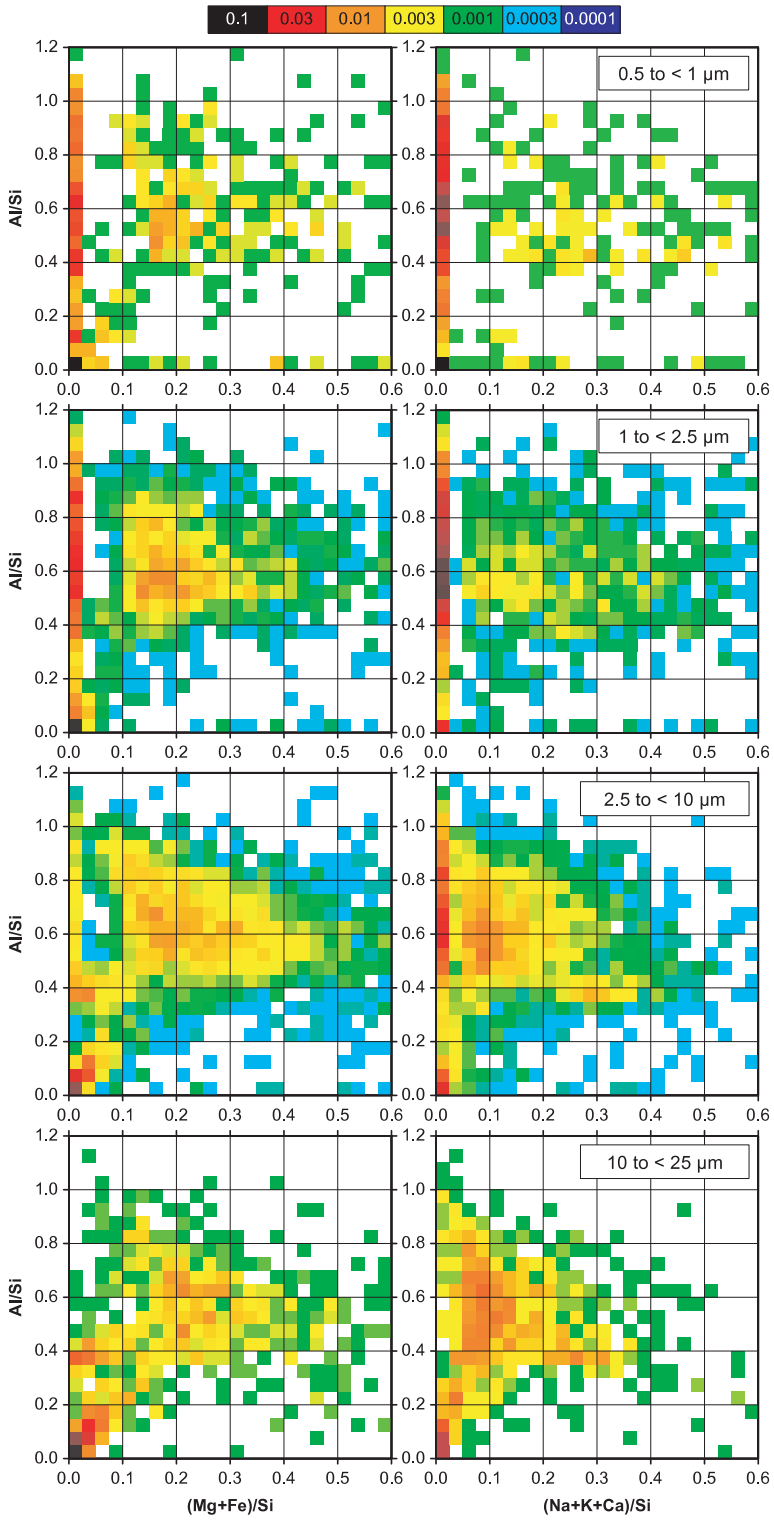

Fig. 5. Normalized element atomic ratio fraction distribution for silicate particles during dust situation at Praia, Cape Verde, as function of particle diameter (diameter ranges are given in the top right of the graphs). For the size ranges of the largest and smallest particles, the particle number was not sufficient to resolve number fractions below 0.001 (blue colours).

without iron content and (d) other particles (mainly sodium chloride and sulphates at Cape Verde and calcium-rich particles and sulphates in Morocco). The general shape of the iron distribution is similar for Praia and Tinfou, with the smallest sizes showing the lowest number of iron-containing particles. The overall number of iron-containing particles is smaller at Praia, especially there is a higher fraction of iron-free particles in the size range below 2.5-µm diameter, as it is to be expected due

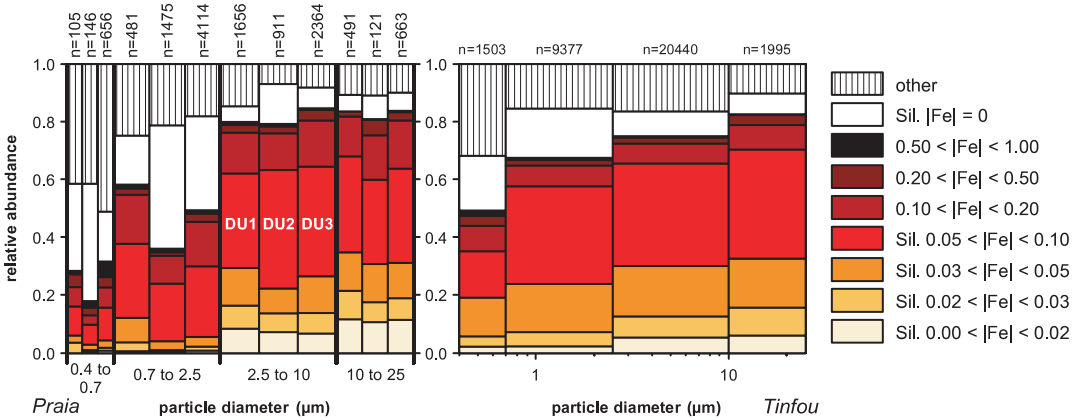

Fig. 6. Particle iron index for the dust phases at Praia in 2008 and at Tinfou, Morocco, in 2006. Particles are classified based on their iron index and chemical classification; classes marked with Sil. are required to be classified into a 'silicates' or the 'quartz' class (Table S1).

to the marine influence. Although the number fraction of silicates with $|Fe| < 0.1$ is similar for both locations for particle sizes larger than 2.5 µm, there is a considerable higher amount of particles with $0.1 < |Fe| < 0.2$ at Praia, especially for particles diameters smaller than 2.5 µm. This can most probably be explained by the more southerly source regions, which provide more iron-rich mineral dust particles (Claquin et al., 1999; Kandler et al., 2007). As a result of this distribution, the average iron index for particles between 1 and 20 µm in diameter increases only slightly between Tinfou (0.053) and Praia (0.064), but there is a significant increase from 0.024 to 0.061, if the average iron index is weighted by particle volume for the same size range. The average iron index is not depending on particle size. Differences between the three dust periods are especially visible in the size range of 0.7–2.5 µm. DU1 exhibits the highest concentrations of iron-containing particles, while DU2 has the lowest. Particularly, the number of iron-free silicates is lowest during DU1 for the mineral dust mode particles. These differences are probably related to differences in source region (cf. Claquin et al., 1999; Kandler et al., 2011).

In addition to iron, phosphorus is one of the limiting nutrients for marine ecosystems (Brunner and Bachofen, 1998) and tropical rain forests (Swap et al., 1992). Mineral dust can be the most important supplier of phosphorus (Carbo et al., 2005). One of the highest phosphorus inputs into the Atlantic ocean west of Africa was recorded east of the Cape Verde region (Baker et al., 2003). In contrast to iron, the average phosphorus index decreases with increasing particle size at Praia as well as at Tinfou (Fig. 7). Assuming that phosphorus is advected within the mineral dust, a size dependent phosphorus volume contribution is estimated as the product of the phosphorus index and the 'advected volume' distribution (Kandler et al., 2011). Despite the decrease in phosphorus index with increasing particle size, the aerosol volume distribution remains dominating, so most of the phosphorus is available in the size range between 2.5 and 10 µm. Table 2 shows the distribution of phosphorus within the single

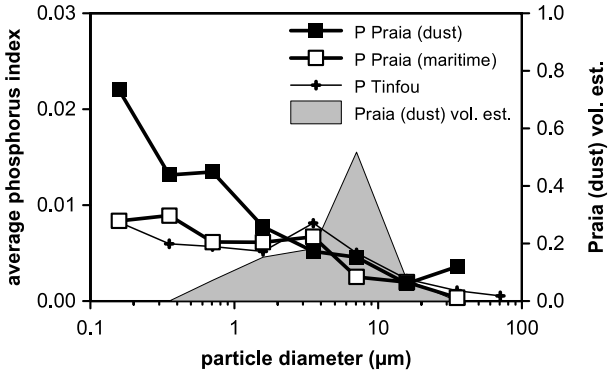

Fig. 7. Average phosphorus index as function of particle size for dust and maritime situations at Praia, Cape Verde, and at Tinfou, Morocco; for the Praia dust situation in addition the volume contribution of phosphorus is shown, which is estimated as product of phosphorus index and 'advected volume' distribution (Kandler et al., 2011).

Table 2. Number fraction and relative volume contribution of particles bearing different amounts of phosphorus at Praia, Cape Verde, Tinfou, Morocco and Izaña, Tenerife.

	Praia mineral dust	Praia maritime	Tinfou	Izaña
Fraction with $\|P\| = 0$	0.845	0.780	0.719	–
Fraction with $\|P\| > 0$	0.155	0.220	0.281	–
Fraction with $0.1 < \|P\| < 0.3$	0.007	0.009	0.004	0.012
Fraction with $\|P\| > 0.3$	0.006	0.001	0.0003	0.0003
P volume with $\|P\| < 0.1$	0.485	0.595	0.742	–
P volume with $0.1 < \|P\| < 0.3$	0.325	0.167	0.258	–
P volume with $\|P\| > 0.3$	0.190	0.238	0.0003	–

The volume contribution is estimated as product of particle volume and phosphorus index. Only phosphorus index values larger than 0.05 could be regarded for Izaña.

particles. About one sixth to one fourth of the particles carry a detectable amount of phosphorus. The number of phosphorus-rich particles (e.g. apatite) is very low. Most of the phosphorus volume contribution is estimated to be present in particles with only trace amounts of phosphorus, which can be either phosphate adsorbed on the surface or small phosphate-rich grains like apatite in an aggregate, for example clay mineral aggregate. From the decreasing *P* index with increasing particle size it can be concluded by reasoning similar to that for sulphate coatings (Falkovich et al., 2001; Kandler et al., 2007) that most of the phosphorus is transported as phosphate adsorbed on the particle surface, although the absolute phosphorus signal in the analysis is too weak for a detailed quantification. This surface adsorption of phosphate, however, is described for clay minerals and iron oxides in soils (Fontes and Weed, 1996; Ioannou and Dimirkou, 1997) and was identified on single particles in samples over the Sahara (Scheuvens et al., 2011).

3.2. *Mixing state*

The mixing state of the aerosol is assessed in two different ways. For particles larger than 500 nm in diameter, where the chemical composition can be determined with a higher accuracy, a ternary mixing model is used. For smaller particles, a manual investigation based on particle morphology was used. Figure 8 shows time series of the aerosol mixing state at Praia in 2008 derived by the ternary mixing model. At the beginning of the campaign during MAR1, the aerosol is dominated by sodium chloride and sulphates. With the onset of DU1, the aerosol becomes dust-dominated. At the end of DU3, the composition of

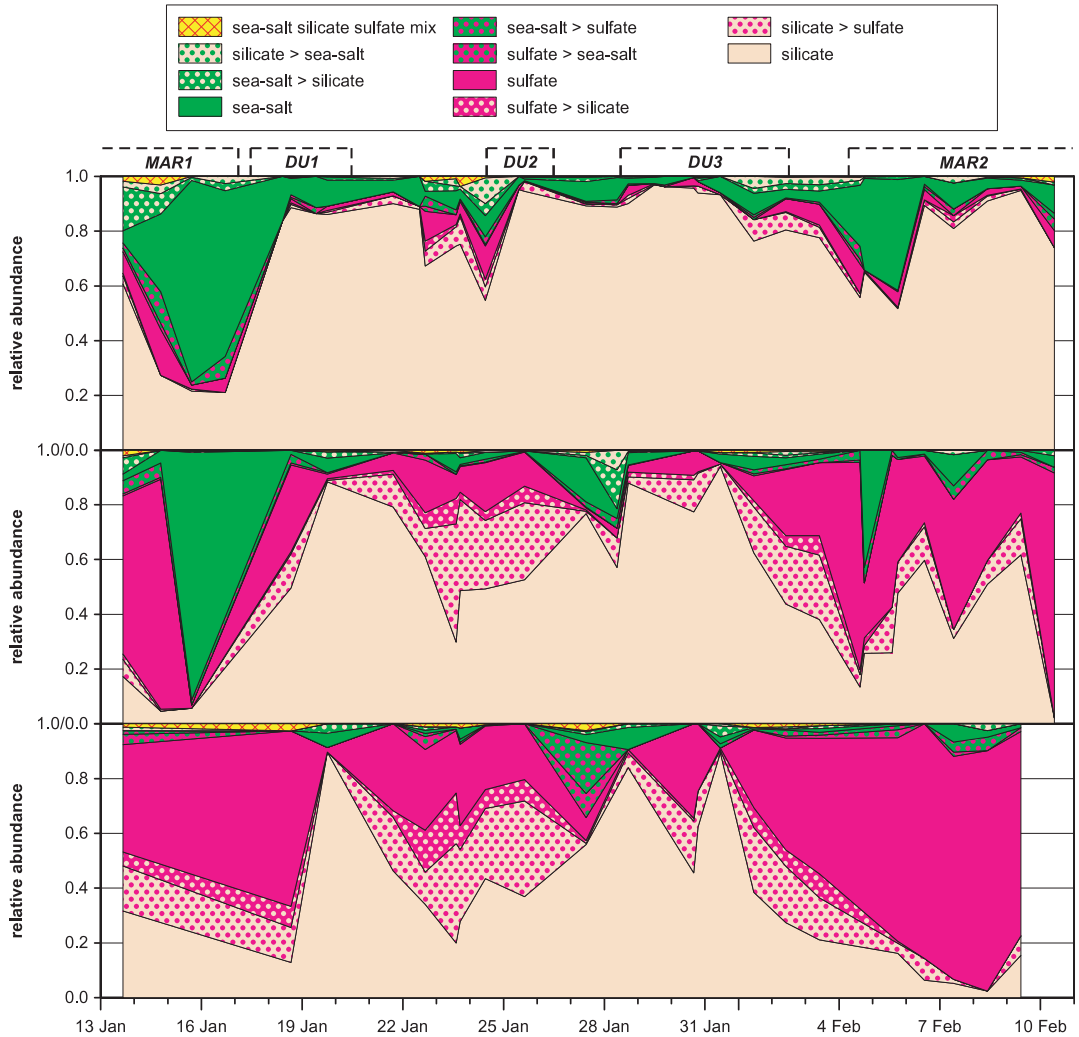

Fig. 8. Time series of particle mixing state derived from chemical composition for the ternary mixing model; particle diameter range 2.5–10 μm (top), 1–2.5 μm (centre) and 0.5–1 μm (bottom). Particles disregarded by the ternary mixing model are not shown in this graph. In addition, the meteorological classification is shown.

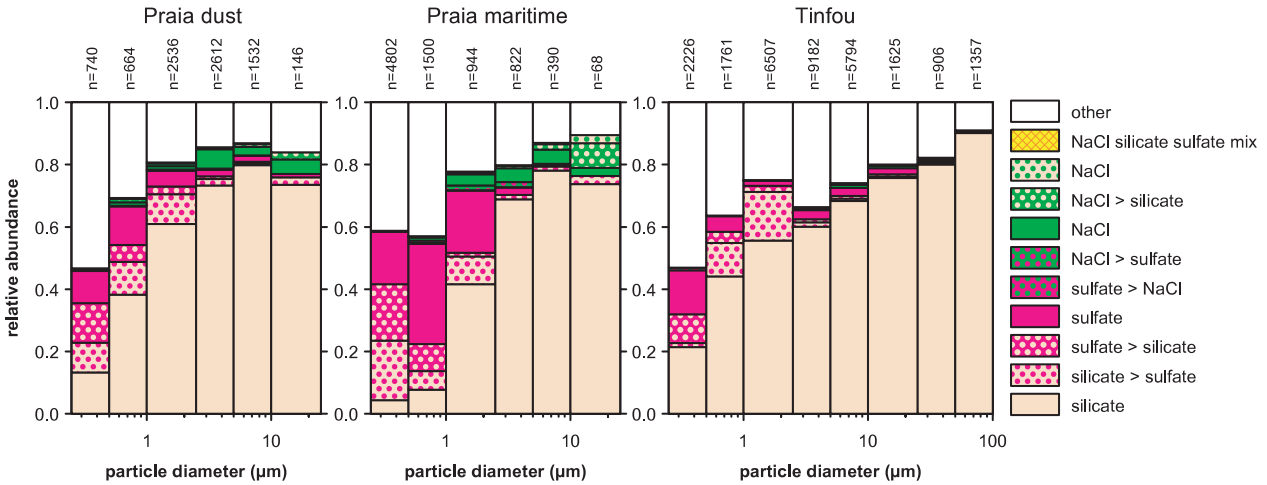

Fig. 9. Particle mixing state assessed by the ternary mixing model for Praia, dust and maritime situations in 2008 as well as for Tinfou, Morocco, in 2006. In addition, the number of particles neglected by the ternary mixing model is shown as 'other'. The number of particles in each size class is shown above the diagram.

the small and large particles differs. Although within the size range below 2.5 µm in particle diameter, non-dust components gain a higher abundance, the large particles are mostly mineral dust. In general, the fraction of internally mixed particle is smallest for the largest particles (Fig. 9, Praia graphs). An internal mixture of mineral dust and chloride is practically absent, in contrast to findings for Asian dust, where this mixture is reported commonly (Zhang et al., 2006; Sullivan et al., 2007). A probable explanation is the difference in meteorology during transport. While towards the Cape Verde islands mineral dust was transported mainly at mid-range relative humidities without cloud processing in the Saharan air layer, towards Japan mineral dust is transported inside the marine boundary layer and, thus, may have experienced significantly higher humidities leading to droplet formation and mineral dust scavenging. Also, only few particles appear as aged sea salt showing sulphur and chlorine content. This can be explained by the vicinity of the sea to the measurement station, so the freshly emitted sea-salt particles always dominated over the aged ones. The only significant internal mixture detected occurred between mineral dust and sulphate. Particles smaller than 2.5 µm are sometimes internally mixed. In these mixtures, the silicon abundance was mostly higher than that of sulphur. From the time series (Fig. 8, middle and lower graph) it becomes apparent that the fraction of mixing is highest when the pure mineral dust abundance decreases, which is visible for DU1 starting from 21 January and for DU3 starting from 29 January and 1 February. This indicates that the internal mixture for the smaller particles occurs in these situations at least partly as result of heterogeneous reactions (e.g. Ullerstam et al., 2002; Usher et al., 2002). The ternary mixture of all three components is extremely rare. This is in analogy to investigations in the Sahelian region (Deboudt et al., 2010), where binary mixtures also were much more frequent than ternary ones.

Comparing the state of mixture for Praia and Tinfou (Fig. 9), it can be seen that in general the internal mixture of mineral dust and sulphate is usually more frequent in Praia than in Tinfou, what could be expected due to the more distant source regions for the Cape Verde islands. However, between 1 and 2.5 µm in particle diameter, a high fraction of silicate particles at Tinfou was internally mixed with sodium sulphate. In addition, the decreasing significance of the simple ternary mixing model towards smaller particle sizes at Cape Verde becomes obvious.

The mixing state of the particles smaller than 500 nm in diameter was investigated for two selected samples by TEM. Figure 10 shows the different types of mixtures found for the dust and maritime situations at Praia. In addition, Table 3 gives a summary of the analysis. Approximately two thirds of the particles have no detectable inclusion. However, nearly all volatile particles left a skin-like remainder (Fig. 10b) after electron bombardment, which could be interpreted as an organic coating of low volatility, as it was amorphous and yielded no chemical signal except carbon. A mixture of mineral dust and amorphous carbonaceous material is described also for the Sahelian region (Deboudt et al., 2010). The thickness of this potential coating was higher for the maritime sample than for the dust sample, appearing as more pronounced outlines and wrinkles in the images. Approximately one third of the particles included or adhered to solid non-volatile material, which was either a core (Figs 10c and d) or attachment (Figs 10e and f) of soot or of mineral dust (Figs 10i and j). Internal mixtures with mineral dust were only found in the dust period sample. Although on average the volume fraction of soot inclusions is much lower than that of mineral dust inclusions, a few nearly pure soot particles were present (Figs 10g and h), which in sum dominated the total soot volume. Mineral dust particles often contained only a small amount of volatile

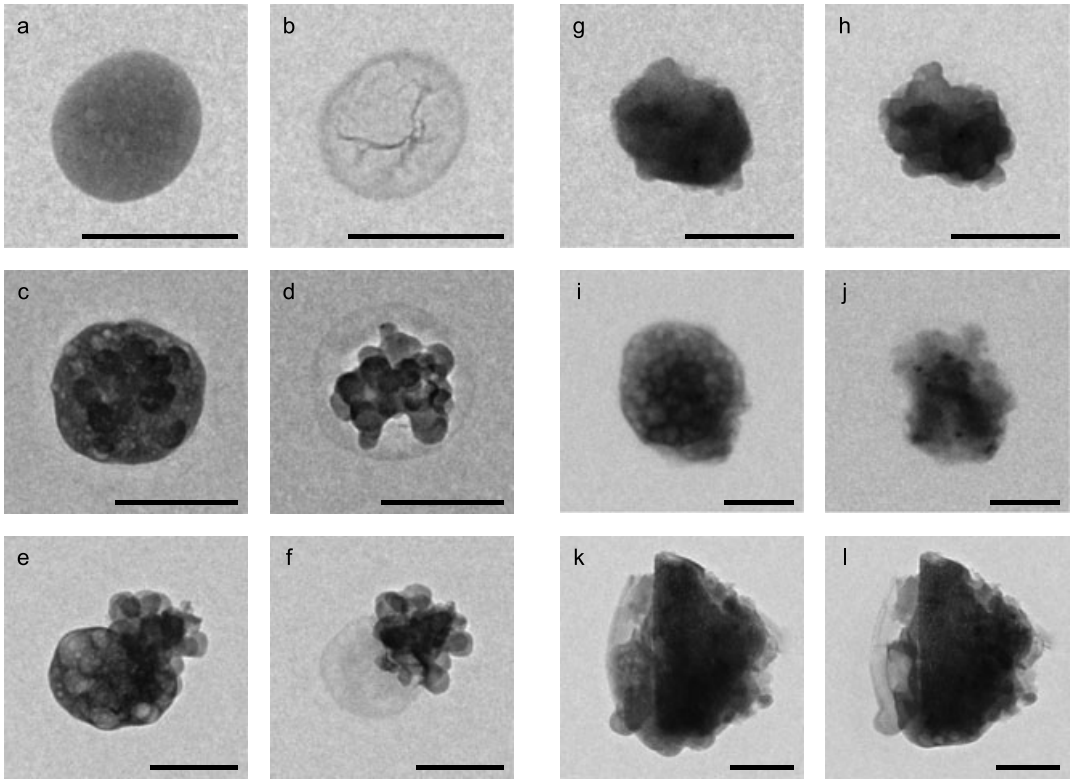

Fig. 10. Internal mixture of submicron particles determined by TEM. The scale bar has a length of 200 nm. The image pairs (a/b, c/d, etc.) show the same particle before and after extensive electron bombardment. a/b: sulphate particle without inclusion, but with a potential organic coating; c/d: sulphate particle with soot inclusion; e/f: soot particle adhering to sulphate particle; g/h: soot particle with a chemically undetermined thin coating; i/j: silicate particle with a sulphate coating, the dark spots are probably iron oxides; k/l: mineral dust particle with only small amounts of volatile material (lower left side of the particle). The particles in c, e and i exhibit already beam damage, but showed a smooth structure of the volatile part at the beginning of the analysis.

material (Figs 10k and l). Obviously, soot as well as mineral dust particles can provide a surface for heterogeneous reactions, although particle coagulation can also contribute to the internal mixture.

3.3. Refractive index

Complex refractive indices have been calculated from the composition and morphological information using a mixture model of pure components. The variation in the real part of the complex refractive index is low. At a wavelength of 532 nm, values between 1.54 and 1.58 were found for maritime, and between 1.55 and 1.61 for dust situations. Significantly more variation is encountered for the imaginary part. The frequency distribution in fractions of the imaginary part of the refractive index as function of the particle size for 467 and 670 nm wavelength at Praia is shown in Fig. 11 for the maritime as well as for the dust situation. The lowest row of colour fields adjacent to the *x*-axis includes the particles, which have zero absorption. A multi-modal distribution is visible in Fig. 11. For particles smaller than 500 nm during the dust situations, two modes are visible at 467 nm wavelength. Between 10^{-3}i and 10^{-2}i there is a mode of mineral dust sulphate mixtures (1), and at the *x*-axis there are pure sulphate particles (2). For larger particles, a large, more absorbing mineral dust mode (3) is visible instead of the mineral dust sulphate mixture mode (1), which shows decreasing modal refractive index values for increasing particle size. On the *x*-axis, non-absorbing sodium sulphate and chloride particles are present (4). In addition, a third mode for large particles (5) becomes visible at 10^{-4}i, consisting mainly of the internal mixtures of mineral dust and sulphate. The latter one disappears towards larger particles. During the maritime situation, qualitatively the same modes are visible. In addition, between 100 and 250 nm particle diameter, a third mode (6) with a high absorption of around 10^{-1}i appears, which is produced by the soot–sulphate mixture particles. In contrast to the dust situation and as it can be expected, the mineral dust mode for particles larger than 1 μm is much less pronounced, and instead the fraction of non-absorbing particles is very high. At 670 nm wavelength, above the haematite absorption edge, the mineral dust mode is moved to lower absorption values by approximately one order of magnitude. As a result, the dust-influenced refractive index modes can

Table 3. Mixing state properties for particles smaller than 600 nm diameter for a mineral dust and a maritime sample determined by transmission electron microscopy.

	Feb 1 (DU3)	Feb 4 (MAR2)
Number of particles	129	84
With one inclusion	41	18
With several inclusions	2	6
Containing soot	27	24
Containing mineral dust	16	0
Overall soot volume fraction	0.03	0.15
Average soot volume fraction for soot-containing particles	0.13	0.29
Overall mineral dust volume fraction	0.23	0
Average mineral dust volume fraction for mineral dust-containing particles	0.67	–
Overall non-refractory volume fraction	0.74	0.85

no longer be distinguished in this graph for all cases. Instead, for the dust situation a small mode of soot-containing particles between 100 and 250 nm in diameter becomes visible at 10^{-1}i (7).

If the refractive indices are weighted according to the particle volume and then averaged, assuming a homogeneous internal mixture of the particulate material, a mean refractive index for each particles size and meteorological situation can be calculated. Table 4 gives these averages for wavelengths between the near ultraviolet and near infrared spectral region. With the same assumption, an overall average can be calculated by applying the measured aerosol size distributions (Kandler et al., 2011) for volume weighting the separate size classes. In Table 4, the imaginary part of the refractive index k is given in 10^{-3}i. For wavelengths smaller than the haematite absorption edge, the size dependence of the absorption is ambiguous. A minimum exists between 250 nm and 1 µm in particle diameter for the dust situation, which is explained by the high sulphate contents in this size range. For wavelengths longer than 600 nm, a decrease in absorption with increasing particle size is obvious, which is strongest at around 1 µm wavelength, where mineral dust has its weakest absorption coefficient. The overall average refractive index is dominated by the mineral dust and is influenced by soot absorption for wavelengths larger than 550 nm. A table of refractive index frequencies for all wavelengths shown in Table 4 is presented in Appendix S1. The calculated average for the dust periods at 630 nm wavelength is within errors identical to those values determined in earlier experiments in the Cape Verde region (Haywood et al., 2003).

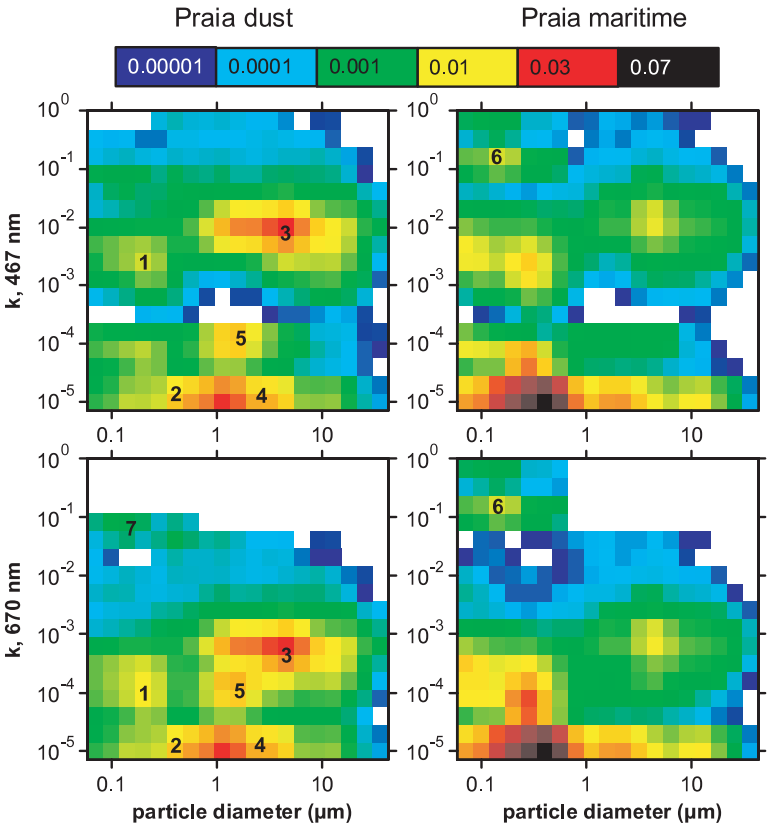

Fig. 11. Distributions of the refractive index imaginary part as function of particle size at 467 and 670 nm wavelength. The frequency of occurrence is normalized to the total number of particles for each meteorological phase. Areas of interest are marked by numbers (see text for details). The raw data leading to this figure are available in the electronic supporting information together with the data for all other regarded wavelengths.

Table 4. Average complex refractive indices $m = n + ik$ derived from chemical composition for the mineral dust and maritime periods at Praia, Cape Verde, in 2008, for different wavelengths (top row) as function of particle size interval.

	Interval (μm)		355 nm		380 nm		441 nm		467 nm		532 nm		630 nm		660 nm		670 nm		869 nm		1021 nm		1638 nm		2000 nm	
	Lower	Upper	n	k^*	n	k^*	n	k^*	n	k^*	n	k^*	n	k^*	n	k^*	n	k^*	n	k^*	n	k^*	n	k^*	n	k^*
Dust	0.05	0.1	1.558	10	1.558	11	1.560	9.6	1.561	8.9	1.562	6.6	1.560	3.2	1.559	3.0	1.559	3.0	1.559	2.9	1.557	2.9	1.558	3.6	1.558	4.1
situation	0.1	0.25	1.553	6.8	1.553	6.9	1.553	6.1	1.554	5.6	1.554	4.2	1.550	2.0	1.550	1.9	1.550	1.9	1.549	1.8	1.548	1.8	1.548	2.3	1.548	2.6
	0.25	0.5	1.607	45	1.605	45	1.608	40	1.610	35	1.615	23	1.606	5.3	1.602	4.3	1.602	3.9	1.597	3.1	1.589	2.9	1.589	3.7	1.587	4.1
	0.5	1	1.572	17	1.571	17	1.571	15	1.573	13	1.574	8.7	1.569	1.4	1.568	0.94	1.568	0.81	1.566	0.46	1.562	0.39	1.561	0.67	1.560	0.77
	1	2.5	1.572	12	1.571	13	1.572	11	1.573	9.9	1.573	6.4	1.571	1.0	1.569	0.70	1.569	0.61	1.568	0.35	1.565	0.31	1.564	0.59	1.563	0.73
	2.5	5	1.582	14	1.581	15	1.581	13	1.582	11	1.583	7.4	1.580	1.2	1.578	0.81	1.578	0.70	1.577	0.40	1.573	0.35	1.572	0.64	1.569	0.80
	5	10	1.577	14	1.576	15	1.576	13	1.577	11	1.578	7.4	1.576	1.2	1.574	0.81	1.574	0.70	1.573	0.40	1.569	0.35	1.568	0.64	1.566	0.81
	10	20	1.573	11	1.572	12	1.571	10	1.572	9.3	1.573	6.0	1.570	0.94	1.569	0.66	1.569	0.57	1.567	0.33	1.563	0.29	1.562	0.55	1.560	0.69
	20	50	1.573	16	1.573	17	1.575	15	1.576	14	1.578	8.8	1.577	1.4	1.576	0.96	1.576	0.83	1.574	0.47	1.570	0.42	1.570	0.75	1.569	0.95
	Volume average		1.577	13	1.576	14	1.575	12	1.576	11	1.577	7.0	1.574	1.1	1.573	0.77	1.573	0.67	1.571	0.38	1.567	0.34	1.564	0.62	1.564	0.78
Maritime	0.05	0.1	1.550	27	1.552	26	1.556	24	1.558	23	1.559	21	1.556	19	1.556	19	1.556	19	1.557	19	1.557	19	1.559	23	1.561	25
situation	0.1	0.25	1.545	25	1.547	24	1.549	22	1.550	22	1.551	20	1.546	19	1.546	19	1.546	19	1.546	19	1.545	19	1.548	23	1.548	25
	0.25	0.5	1.543	9.3	1.543	8.9	1.543	8.2	1.543	7.9	1.543	7.2	1.535	6.5	1.535	6.5	1.535	6.4	1.535	6.5	1.534	6.6	1.535	7.9	1.535	8.7
	0.5	1	1.547	4.5	1.545	4.8	1.544	4.3	1.545	3.8	1.544	2.5	1.537	0.52	1.536	0.40	1.536	0.37	1.535	0.27	1.534	0.26	1.534	0.43	1.533	0.43
	1	2.5	1.555	10	1.553	11	1.554	9.8	1.555	8.8	1.555	5.7	1.549	0.88	1.548	0.60	1.548	0.51	1.547	0.28	1.544	0.23	1.544	0.45	1.543	0.47
	2.5	5	1.576	17	1.574	18	1.576	16	1.577	14	1.578	9.2	1.576	1.4	1.574	0.99	1.574	0.84	1.572	0.47	1.568	0.40	1.567	0.71	1.566	0.86
	5	10	1.572	15	1.570	16	1.570	14	1.571	12	1.572	7.9	1.568	1.2	1.566	0.84	1.566	0.72	1.564	0.40	1.561	0.34	1.560	0.62	1.559	0.72
	10	20	1.566	11	1.564	12	1.564	10	1.565	9.0	1.565	5.8	1.560	0.91	1.559	0.63	1.559	0.54	1.557	0.30	1.554	0.26	1.554	0.50	1.553	0.58
	20	50	1.573	16	1.572	17	1.573	15	1.575	13	1.576	8.5	1.575	1.3	1.573	0.93	1.573	0.80	1.571	0.45	1.568	0.40	1.567	0.72	1.566	0.89
	Volume average		1.572	14	1.570	14	1.571	13	1.572	11	1.571	7.4	1.567	1.2	1.566	0.87	1.566	0.76	1.564	0.46	1.558	0.41	1.553	0.70	1.559	0.83

k^* is the imaginary part $k \times 1000$. For each size class, the values are calculated as volume-weighted average. The overall volume average is weighted with the measured size distributions (Kandler et al., 2011).

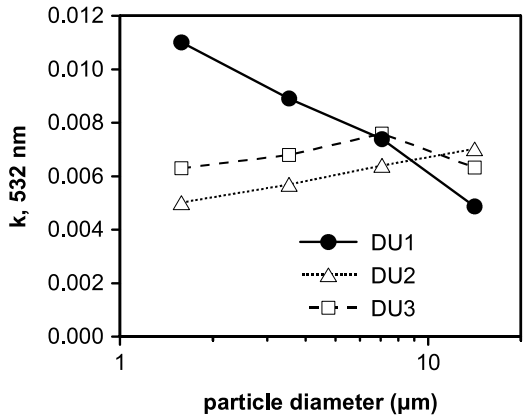

Fig. 12. Imaginary part of refractive index at 532 nm wavelength as function of particle size in the dust advection size regime for the three dust periods.

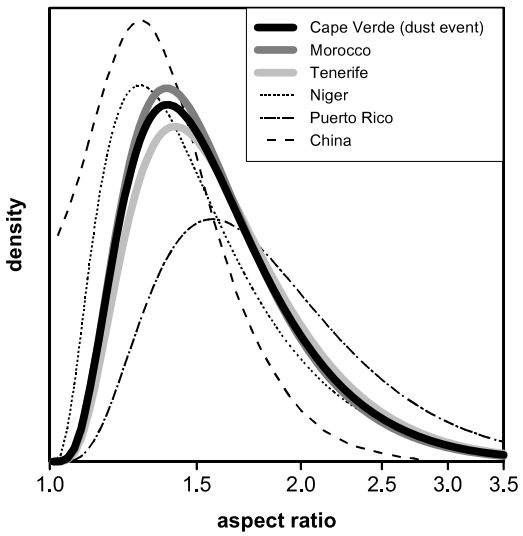

Fig. 13. Parameterized dry aspect ratio density distributions for the SAMUM campaigns at Tenerife, Morocco and Cape Verde dust event (thick lines) as well as distributions compiled from literature for China (Okada et al., 2001), Niger (Chou et al., 2008), and Puerto Rico (Reid et al., 2003a).

Although in terms of composition class abundance no difference between the single dust periods could be observed, the situation is different for the refractive index. The average imaginary part of the refractive index at 532 nm wavelength for the three dust periods as function of particle diameter in the main mineral dust advection size range is shown in Fig. 12. Although the periods DU2 and DU3 show a very similar size relation, DU1 exhibits significantly larger values for particles smaller than 5 μm in diameter. This is in accordance with the source regions for the dust periods, which were similar for DU2 and DU3 (Mali/Niger, see Knippertz et al., 2011), but different for DU1 (Mauritania). For larger particles, however, all three dust periods have very similar absorption values.

A comparison of these chemistry-derived refractive indices with values derived from optical measurements at Praia ground station is discussed elsewhere (Müller et al., 2011).

3.4. Particle shape

The shape of the particles is determined in terms of the two-dimensional aspect ratio. The distribution of the aspect ratios at Cape Verde can be described by a modified log-normal distribution (Kandler et al., 2007) with high accuracy:

$$h(\mathrm{AR}) = \frac{1}{\sqrt{2\pi}\sigma(AR-1)} \times \exp\left(-\frac{1}{2}\left(\frac{\ln(AR-1)-\mu}{\sigma}\right)^2\right) \quad (4)$$

with σ and μ the distribution parameters.

The shape of the overall distribution (Fig. 13) is very similar to measurements at other locations. Although the average distributions do not show a significant difference between Cape Verde, Morocco and Tenerife, slightly more spherical particles have been reported for Niger (Chou et al., 2008) and China (Okada et al., 2001). In contrast, more elongated particles were found in the long-range transport of Saharan dust at Puerto Rico (Reid et al., 2003a).

The size-resolved aspect ratio distribution for dry particles (Fig. 14) shows significant differences between the dust and maritime situations in Praia, reflecting the compositional change, whereas the dust situation in Praia is similar to the average measurements at Tinfou. In both situations, the particles smaller than approximately 700 nm are more spherical than the larger ones with median aspect ratios below 1.4. However, the distribution is narrower in the maritime case, showing the absence of small elongated mineral dust particles. Towards the smallest particles the aspect ratio increases, showing at least in part presence of fractal soot particles, but the measurements have a higher uncertainty for these particles due to limiting instrument lateral resolution at the used magnifications. For particle larger than 700 nm the aspect ratio increases to stable median values between 1.6 and 1.7 for the Praia dust case and the average of the measurements at Tinfou. The same values are found for the maritime case at particle sizes larger than 2.5 μm. For particles between 700 nm and 2.5 μm in the maritime situation, significantly higher median aspect ratio values reaching more than 1.9 are observed in conjunction with a very wide distribution of these values. A more detailed analysis of these particles with high aspect ratios in terms of composition is shown in Fig. 15. Three different populations are visible: silicate particles with dust-like aspect ratios between 1.5 and 2, medium sulphur indices and low sodium indices, sodium chloride particles with low aspect ratios below 1.5, low sulphur, but high sodium

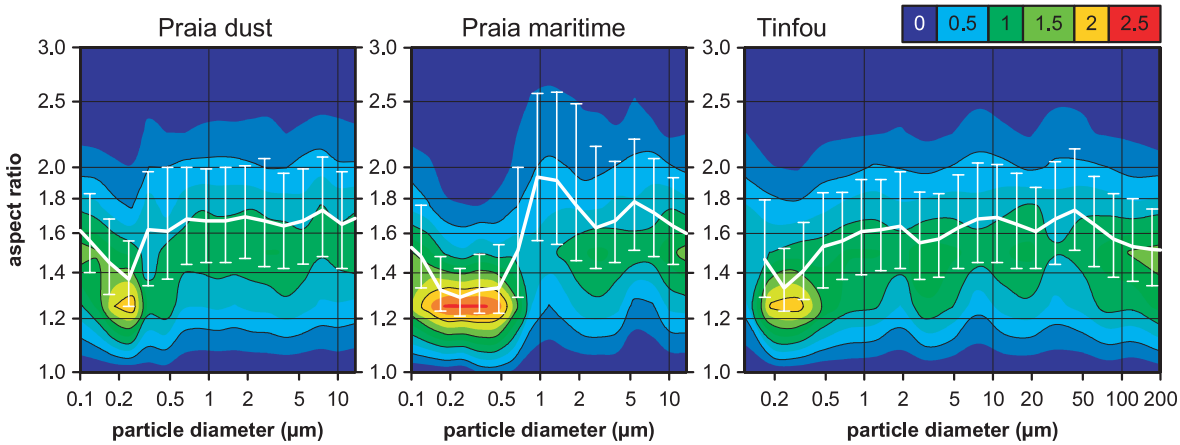

Fig. 14. Aspect ratio density distributions for dry particles at Praia for dust and maritime situations and at Tinfou, Morocco. The white curve shows the median and the interquartile range as function of particle size.

indices, and, finally, particles with high aspect ratios between 1.5 and 5, high sulphur and high sodium indices. The latter sodium sulphate particles are obviously present as needle-like crystals, which were also observed at other locations (Kandler et al., 2007; Coz et al., 2009). Taking into account the potential deliquescence and efflorescence behaviour of pure salts during the measurement campaign (Fig. 2), it can be concluded that these high aspect ratios in the dry state are in part representative for the investigated aerosol, depending on the humidity history of the particles. However, small amounts of $NaHSO_4$ would significantly decrease particularly the efflorescence relative humidity (Tang, 1996), so no final conclusion can be drawn on the solution state of the sodium sulphate particles at Praia. Relating the particle shape to the particle sulphur index, Fig. 16 shows that while in Tenerife there was a monotonous dependency between *AR* and |S|, in Morocco as well as at Cape Verde high values of |S| can lead to very high as well as very low values of *AR*. This ambiguous behaviour is associated with the difference of ammonium sulphate and sodium(-potassium-calcium)-sulphates, of which the former ones tend to be present in particles with low AR, whereas the latter ones show a high AR, as it was already discussed earlier (Kandler et al., 2009). Although in Morocco different values of AR in the most-populated region between 1.3 and 2.5 exhibit the same values of |S|—i.e. the sulphur index has no influence on particle shape in this regime—there was an increase in |S| recorded at Tenerife and Cape Verde, indicating that an addition of sulphate to the particles increases its elongation in the dry state. It may be speculated that this different behaviour points to different mechanisms of sulphate uptake or differences in the humidity history of the particles, leading to faster or slower recrystallization and, thus, different shape. In Fig. 16, the AR–|S| relationship at Cape Verde appears as combination of Tenerife and Morocco, but with elevated absolute values of |S|, indicating higher average sulphate contents. When the AR is calculated separately for single

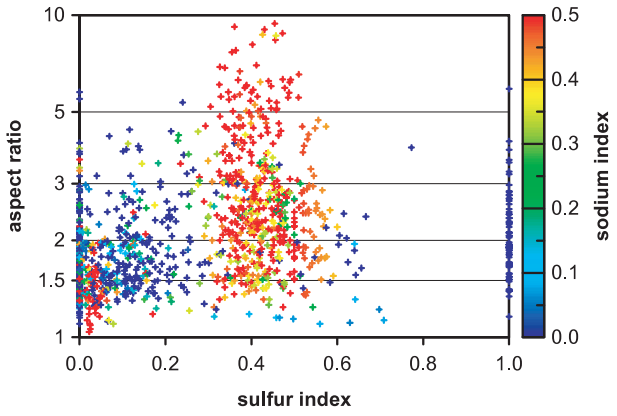

Fig. 15. Aspect ratio as function of particle sulphur index for particles between 0.8 and 1.5 µm diameter at Praia during the maritime situations. The particle sodium index is shown as colour coding.

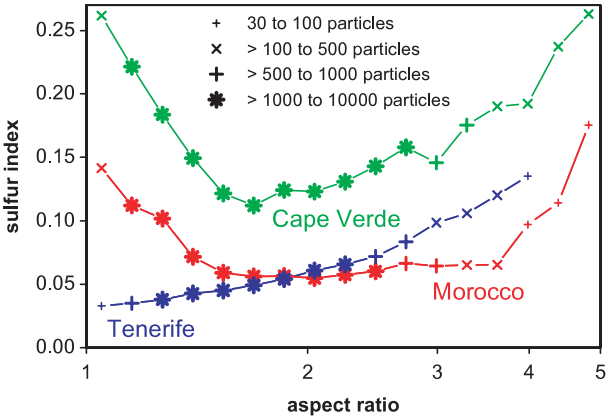

Fig. 16. Dry aspect ratio as function of particle sulphur index for all particles collected at Izaña, Tenerife, in 2005, at Tinfou, Morocco, in 2006, and at Praia, Cape Verde, in 2008. The number of particles in a particular aspect ratio interval in shown as different symbols.

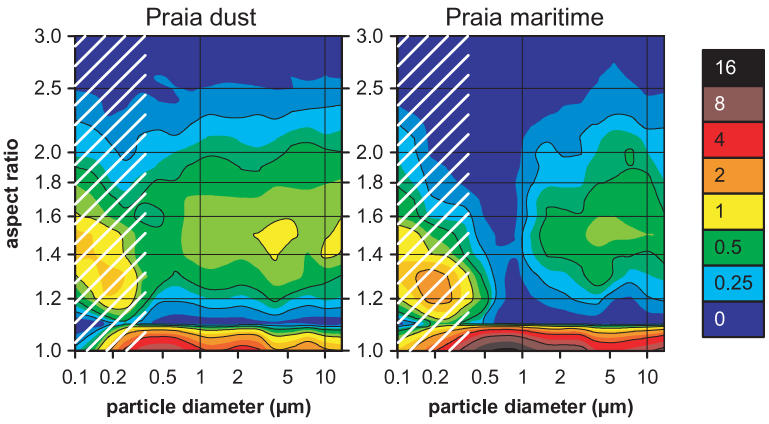

Fig. 17. Aspect ratio density distributions for wet particles (85% relative humidity) at Praia for dust and maritime situations. In the shaded area, the ratio of abundance of non-spherical to spherical particles has a high uncertainty.

particle types, small differences become visible; however, as the results are not significantly different from other locations (Kandler et al., 2007; Coz et al., 2009; Kandler et al., 2009), they are not shown here.

To simulate the shape under highly humid conditions, a solution and growth model for 85% relative humidity was applied to the chemical and shape measurements. Figure 17 shows the simulated size-resolved aspect ratio distributions for the aerosol during the dust and the maritime situations. For both situations in the size range larger than 1 µm particle diameter, two modes of particle aspect ratio are present, a spherical mode of soluble salts (sodium chloride and sulphate) and a mineral dust mode. Naturally, during the dust situations the mineral dust mode has a significantly higher abundance. The mineral dust mode extends also to smaller particle sizes of 500 nm during the dust situation, while in the maritime situation between 500 nm and 1 µm particle diameter only spherical particles are present. Smaller than 500 nm in particle diameter, again two modes of particle aspect ratio are visible. In this size range, however, the relative intensity of the two modes is highly uncertain as the chemical signal for these small particles is weak and can lead to misclassification in terms of content of soluble material.

Parameters for the aspect ratio distributions for different particle size regimes and meteorological situations are shown in Table 5 for use in eq. (4). As mentioned, the coefficient of determination r^2 is usually high for the average aspect ratio density distribution. Before parameterization, the aspect ratio distributions were averaged over homogeneous size regimes identified in the data. The last column shows the number fraction of non-spherical particles, that is for which the parameterization is applicable.

Table 5. Parameters of aspect ratio density distributions for the size regimes identified from Figs 14 and 17.

Situation	Diameter range (μm)	σ	μ	r^2	$f_{AR>1}$
Dust—dry particles	0.05–0.15	0.5149	−0.4902	0.97	1
	0.15–0.5	0.6691	−0.7902	0.97	1
	0.5–50	0.6047	−0.3924	0.99	1
Maritime—dry particles	0.05–0.15	0.6093	−0.5576	0.95	1
	0.15–0.6	0.5315	−1.1885	0.98	1
	0.6–2	0.7807	−0.2799	0.99	1
	2–50	0.5997	−0.4040	0.98	1
Dust—wet particles	0.3–0.7	0.6771	−0.3936	0.96	0.60
	0.7–3	0.5800	−0.3994	0.98	0.77
	3–50	0.6024	−0.3867	0.99	0.87
Maritime—wet particles	0.3–0.5	0.5867	−1.1940	0.96	0.43
	0.5–1	0.8476	−0.4480	0.94	0.10
	1–3	0.5817	−0.3732	0.97	0.42
	3–50	0.5962	−0.3316	0.96	0.61

r is the correlation coefficient of the parameterization. $f_{AR>1}$ is the number fraction of non-spherical particles. See text for more details.

4. Summary and conclusions

During the SAMUM-2 field campaign in winter 2008 a thorough characterization of the aerosol at Praia, Cape Verde, was performed by electron-microscopical single particle analysis. The chemical composition of the aerosol is strongly size-dependent, and three size regions with different composition were identified. Particles smaller than 500 nm in diameter consist during dust periods mainly of sulphate and mineral dust. Between 500 nm and 2.5 μm, a transition range with increasing abundance of mineral dust towards larger particles is observed. Larger than 2.5 μm in diameter, the aerosol is dominated by mineral dust. In addition, there is always a background of marine aerosol present at Cape Verde. This size dependency stays basically the same for maritime situations with—of course—a higher abundance of marine aerosol. In addition, the transition regime seems to be shifted towards larger particles, which is probably connected to a higher abundance of sodium sulphate. The maritime situations exhibit a higher variability in composition than the dust periods, but except for a few measurements even during maritime situations there is always a large contribution of mineral dust to the aerosol.

The mineral dust component at Cape Verde is dominated by silicates. From their chemical fingerprint, three different types of silicates were distinguished: quartz, feldspars and clay mineral aggregates. The most abundant silicate group is the clay mineral aggregate group, which also shows the highest chemical variability. Because of this high variability, no significant differences between the dust and maritime periods as well as between Cape Verde and Morocco could be detected. However, there is a change in group abundance with particle size; as it is to be expected, with increasing particle size the abundance of the feldspars and quartz increases in the aerosol.

Compared to Morocco, mainly the abundance of calcium-rich particles is much lower at Cape Verde in accordance with the source situation. A difference in the silicate composition between Cape Verde and Morocco could not be detected by electron microscopy, although a transition from kaolinite- to illite-dominated mineral dust was clearly identified by X-ray diffraction analysis (Kandler et al., 2011). This emphasizes the importance of the simultaneous deployment of different analytical techniques for the aerosol characterization.

The distribution of iron among the particles is different for aerosol at Cape Verde and Morocco. Especially in the size range 0.7–2.5 μm, significantly higher iron indices are associated with the silicate particles. In general, there is also a higher total iron content of the aerosol at Cape Verde, affecting the modelled radiation absorption.

Assuming a constant size-independent ratio between total and bio-available iron or phosphorus content, respectively, it can be concluded that the major input of both elements into the ocean occurs by particles between 2.5 and 10 μm in diameter.

The abundance of internal mixtures of different aerosol types at Cape Verde is surprisingly low, except for mineral dust mixtures with sulphate and for soot mixtures with sulphate. Internal mixtures are more frequently observed among small particles than among large ones. There is no significant increase in internal mixtures between the source-near aerosol in Morocco and transported mineral dust at Cape Verde. Internal mixtures between mineral dust and sea-salt are observed to a minor extent during maritime periods, whereas an internal mixture between mineral dust and soot was not detected. However, for many small particles there seems to exist an organic coating. The abundance of mineral dust sulphate mixtures appears to increase after the peak of the dust events, leading to the hypothesis that comparatively pristine mineral dust is transported out of the continent, followed by subsequent aging over the ocean. However, the data basis is too sparse to reliably support this hypothesis, and more measurements are needed to assess this process.

The refractive indices were modelled from the chemical composition. Although generally the variation for the real part is low, the imaginary parts exhibit complex multi-modal distributions as function of particle size and meteorological situation. Separate modes (depending on the wavelength) of absorbing mineral dust, mineral dust mixed with sulphate, non-absorbing mineral dust, sulphates and chlorides and soot are visible. The main mode of absorbing mineral dust in the super micron size range shows a decreasing imaginary part with increasing particle size. During the maritime periods, a much higher abundance of non-absorbing particles is present, but also a significantly higher amount of highly absorbing soot is observed. Soot mainly impacts the absorption for wavelengths longer than the haematite absorption edge, whereas for shorter wavelengths mineral dust is dominating. Nitrate and organic components could not be regarded for refractive index determination, but it can be assumed that their impact on the overall refractive index is low (a) due to their most probably small volume contribution and (b) due to comparatively low light absorption (Hoffer et al., 2006; Schkolnik et al., 2007). However, absorption amplification effects (e.g. Schnaiter et al., 2005; Worringen et al., 2008) cannot be regarded by our model.

The shape of the particles was found to be very similar to that of earlier measurements of Saharan dust. Depending on the meteorological situation, three to four size ranges of aspect ratio were observed. Different aspect ratio distributions were found for humid and dry situations. As conclusion, even in a dust-domination region like Cape Verde, in the presence of soluble salts the relative humidity as well as its history must be known to determine shape distributions representative for the investigated location at a given time.

5. Acknowledgments

Financial support by the Deutsche Forschungsgemeinschaft (research group SAMUM, FOR539) is gratefully acknowledged.

We thank TACV-Cabo Verde Airlines and Mr. António Lima Fortes for great logistic support. We are grateful for the extraordinary preparations of the equipment provided by Berthold Friederich, Christian von Glahn and by the workshops of the IPA, Mainz. Finally, we thank the two anonymous reviewers for their useful comments.

References

Alastuey, A., Querol, X., Castillo, S., Escudero, M., Avila, A. and co-authors. 2005. Characterisation of TSP and PM2.5 at Izaña and Sta. Cruz de Tenerife (Canary Islands, Spain) during a Saharan Dust Episode (July 2002). *Atmos. Environ.* **39**, 4715–4728.

Almeida-Prieto, S., Blanco-Méndez, J. and Otero-Espinar, F. J. 2007. Microscopic image analysis techniques for the morphological characterization of pharmaceutical particles: influence of the software, and the factor algorithms used in the shape factor estimation. *Eur. J. Pharm. Biopharm.* **67**, 766–776.

Andreae, M. O. and Rosenfeld, D. 2008. Aerosol–cloud–precipitation interactions. Part 1. The nature and sources of cloud-active aerosols. *Earth-Sci. Rev.* **89**, 13–41.

Ansmann, A., Petzold, A., Kandler, K., Tegen, I., Wendisch, M. and co-authors. 2011. Saharan mineral dust experiments SAMUM-1 and SAMUM-2: what have we learned? *Tellus* **63B**, this issue.

Anthony, J. W., Bideaux, R. A., Bladh, K. W. and Nichols, M. C. 2003. *Handbook of Mineralogy*. Mineral Data Publishing, Tucson, Arizona.

Armstrong, J. T. 1991. Quantitative elemental analysis of individual microparticles with electron beam instruments. In: *Electron Probe Quantitation* (eds. Heinrich, K.F.J. and Newbury, D.E.). Plenum Press, New York, 261–315.

Baker, A. R., Kelly, S. D., Biswas, K. F., Witt, M. and Jickells, T. D. 2003. Atmospheric deposition of nutrients to the Atlantic Ocean. *Geophys. Res. Lett.* **30**, 2296, OCE 11-1-OCE 11-4, doi: 10.1029/2003GL018518.

Barthelmy, D. 2010. Mineralogy database. Available at: http://www.webmineral.com. Accessed on 26-Aug-2010.

Bauer, S. E., Mishchenko, M. I., Lacis, A. A., Zhang, S., Perlwitz, J. and co-authors. 2007. Do sulfate and nitrate coatings on mineral dust have important effects on radiative properties and climate modeling? *J. Geophys. Res.* **112**, 1–9, D06307, doi: 10.1029/2005JD006977.

Bergstrom, R. W., Russell, P. B. and Hignett, P. 2002. Wavelength dependence of the absorption of black carbon particles: predictions and results from the TARFOX experiment and implications for the aerosol single scattering albedo. *J. Atmos. Sci.* **59**, 567–577.

Blanco, A., De Tomasi, F., Filippo, E., Manno, D., Perrone, M. R. and co-authors. 2003. Characterization of African dust over southern Italy. *Atmos. Chem. Phys.* **3**, 2147–2159.

Brunner, U. and Bachofen, R. 1998. The biogeochemical cycles of phosphorus: a review of local and global consequences of the atmospheric input. *Toxicol. Environ. Chem.* **67**, 171–188.

Carbo, P., Krom, M. D., Homoky, W. B., Benning, L. G. and Herut, B. 2005. Impact of atmospheric deposition on N and P geochemistry in the southeastern Levantine basin. *Deep-Sea Res. II* **52**, 3041–3053.

Carlson, T. N. and Benjamin, S. G. 1980. Radiative heating rates for Saharan dust. *J. Atmos. Sci.* **37**, 193–213.

Chang, H. and Charalampopoulos, T. T. 1990. Determination of the wavelength dependence of refractive indices of flame soot. *Proc. R. Soc. Lond. A Math. Phys. Sci.* **430**, 577–591.

Chou, C., Formenti, P., Maille, M., Ausset, P., Helas, G. and co-authors. 2008. Size distribution, shape, and composition of mineral dust aerosols collected during the African Monsoon Multidisciplinary Analysis Special Observation Period 0: dust and biomass-burning experiment field campaign in Niger, January 2006. *J. Geophys. Res.* **113**, 1–17, D00C10, doi: 10.1029/2008JD009897.

Claquin, T., Schulz, M. and Balkanski, Y. J. 1999. Modeling the mineralogy of atmospheric dust sources. *J. Geophys. Res.* **104**, 22243–22256.

Coz, E., Gómez-Moreno, F. J., Pujadas, M., Casuccio, G. S., Lersch, T. L. and co-authors. 2009. Individual particle characteristics of North African dust under different long-range transport scenarios. *Atmos. Environ.* **43**, 1850–1863.

Deboudt, K., Flament, P., Choël, M., Gloter, A., Sobanska, S. and co-authors. 2010. Mixing state of aerosols and direct observation of carbonaceous and marine coatings on African dust by individual particle analysis. *J. Geophys. Res.* **115**, 1–14, D24207, doi: 10.1029/2010JD013921.

DeMott, P., Sassen, K., Poellot, M., Baumgardner, D., Rogers, D. and co-authors. 2003. African dust aerosols as atmospheric ice nuclei. *Geophys. Res. Lett.* **30**, 1732, ASC 1-1-ASC 1-4, doi: 10.1029/2003GL017410.

Durant, A. J., Harrison, S. P., Watson, I. M. and Balkanski, Y. 2009. Sensitivity of direct radiative forcing by mineral dust to particle characteristics. *Prog. Phys. Geog.* **33**, 80–102.

Eldridge, J. E. and Palik, E. D. 1985. Sodium chloride (NaCl). In: *Handbook of Optical Constants of Solids I* (ed. Palik, E.D.). Academic Press, San Diego, 775–793.

Falkovich, A. H., Ganor, E., Levin, Z., Formenti, P. and Rudich, Y. 2001. Chemical and mineralogical analysis of individual mineral dust particles. *J. Geophys. Res.* **106**, 18029–18036.

Fontes, M. P. F. and Weed, S. B. 1996. Phosphate adsorption by clays from Brazilian Oxisols: relationships with specific surface area and mineralogy. *Geoderma* **72**, 37–51.

Formenti, P., Rajot, J. L., Desboeufs, K., Caquineau, S., Chevaillier, S. and co-authors. 2008. Regional variability of the composition of mineral dust from western Africa: Results from the AMMA SOP0/DABEX and DODO field campaigns. *J. Geophys. Res.* **113**, 1–12, D00C13, doi: 10.1029/2008JD009903.

Garrison, V. H., Shinn, E. A., Foreman, W. T., Griffin, D. W., Holmes, C. W. and co-authors. 2003. African and Asian dust: from desert soils to coral reefs. *BioScience* **53**, 469–480.

Garrison, V. H., Foreman, W. T., Genualdi, S., Griffin, D. W., Kellogg, C. A. and co-authors. 2006. Saharan dust—a carrier of persistent organic pollutants, metals and microbes to the Caribbean? *Rev. Biol. Trop. (Int. J. Trop. Biol.)* **54**, 9–21.

Gibson, E. R., Gierlus, K. M., Hudson, P. K. and Grassian, V. H. 2007. Generation of internally mixed insoluble and soluble aerosol particles to investigate the impact of atmospheric aging and heterogeneous processing on the CCN activity of mineral dust aerosol. *Aerosol Sci. Technol.* **41**, 914–924.

Haywood, J., Francis, P., Osborne, S., Glew, M., Loeb, N. and co-authors. 2003. Radiative properties and direct radiative effect of Saharan dust measured by the C-130 aircraft during SHADE: 1. Solar spectrum. *J. Geophys. Res.* **108**, 8577, SAH 4-1-SAH 4-16, doi: 10.1029/2002JD002687.

Heintzenberg, J. 2009. The SAMUM-1 experiment over Southern Morocco: overview and introduction. *Tellus* **61B**, 2–11.

Hoffer, A., Gelencser, A., Guyon, P., Kiss, G., Schmid, O. and co-authors. 2006. Optical properties of humic-like substances (HULIS) in biomass-burning aerosols. *Atmos. Chem. Phys.* **6**, 3563–3570.

Hoornaert, S., Godoi, R. H. M. and Grieken, R. V. 2003. Single particle characterisation of the aerosol in the marine boundary layer and free troposphere over Tenerife, NE Atlantic, during ACE-2. *J. Atmos. Chem.* **46**, 271–293.

Ioannou, A. and Dimirkou, A. 1997. Phosphate adsorption on hematite, kaolinite, and kaolinite-hematite (k-h) systems as described by a constant capacitance model. *J. Colloid Interface Sci.* **192**, 119–128.

Ivlev, L. S. and Popova, S. I. 1972. Optical constants of substances of atmospheric aerosol. *Izv. Vuz. Fiz.* **5**, 91–97.

Jaenicke, R. and Junge, C. 1967. Studien zur oberen Grenzgröße des natürlichen Aerosols. *Beitr. Phys. Atmos./Contrib. Atmos. Phys.* **40**, 129–143.

Jaenicke, R. and Schütz, L. 1978. Comprehensive study of physical and chemical properties of the surface aerosols in the Cape Verde Islands region. *J. Geophys. Res.* **83**, 3585–3599.

Jickells, T. D., An, Z. S., Andersen, K. K., Baker, A. R., Bergametti, G. and co-authors. 2005. Global iron connection between desert dust, ocean biogeochemistry, and climate. *Science* **308**, 67–71.

Kandler, K. 2009. A miniature impactor for aerosol collection with emphasis on single particle analysis. In: *European Aerosol Conference* Karlsruhe, Germany, T092A004.

Kandler, K., Benker, N., Bundke, U., Cuevas, E., Ebert, M. and co-authors. 2007. Chemical composition and complex refractive index of Saharan Mineral Dust at Izaña, Tenerife (Spain) derived by electron microscopy. *Atmos. Environ.* **41**, 8058–8074.

Kandler, K., Schütz, L., Deutscher, C., Hofmann, H., Jäckel, S. and co-authors. 2009. Size distribution, mass concentration, chemical and mineralogical composition, and derived optical parameters of the boundary layer aerosol at Tinfou, Morocco, during SAMUM 2006. *Tellus* **61B**, 32–50.

Kandler, K., Schütz, L., Jäckel, S., Lieke, K., Emmel, C. and co-authors. 2011. Ground-based off-line aerosol measurements at Praia, Cape Verde, during the Saharan Mineral Dust Experiment: Microphysical properties and mineralogy. *Tellus* **63B**, this issue.

Karickhoff, S. W. and Bailey, G. W. 1973. Optical absorption spectra of clay minerals. *Clay Clay Miner.* **21**, 59–70.

Kelly, J. T., Chuang, C. C. and Wexler, A. S. 2007. Influence of dust composition on cloud droplet formation. *Atmos. Environ.* **41**, 2904–2916.

Knippertz, P., Tesche, M., Heinold, B., Kandler, K., Toledano, C. and co-authors. 2011. Dust mobilization and aerosol transport from West Africa to Cape Verde—a meteorological overview of SAMUM-2. *Tellus* **63B**, this issue.

Koren, I., Kaufman, Y. J., Washington, R., Todd, M. C., Rudich, Y. and co-authors. 2006. The Bodélé depression: a single spot in the Sahara that provides most of the mineral dust to the Amazon forrest. *Environ. Res. Lett.* **1**, 1–5, 014005, doi: 10.1088/1748-9326/1/1/014005.

Laskin, A., Cowin, J. P. and Iedema, M. J. 2006. Analysis of individual environmental particles using modern methods of electron microscopy and X-ray microanalysis. *J. Electron. Spectrosc. Relat. Phenom.* **150**, 260–274.

Lázaro, F. J., Gutiérrez, L., Barrón, V. and Gelado, M. D. 2008. The speciation of iron in desert dust collected in Gran Canaria (Canary Islands): combined chemical, magnetic and optical analysis. *Atmos. Environ.* **42**, 8987–8996.

Lieke, K., Kandler, K., Scheuvens, D., Emmel, C., Von Glahn, C. and co-authors. 2011. Particle chemical properties in the vertical column based on aircraft observations in the vicinity of Cape Verde islands. *Tellus* **63B**, this issue.

Mahowald, N. M., Yoshioka, M., Collins, W. D., Conley, A. J., Fillmore, D. W. and co-authors. 2006. Climate response and radiative forcing from mineral aerosols during the last glacial maximum, pre-industrial, current and doubled-carbon dioxide climates. *Geophys. Res. Lett.* **33**, 1–4, L20705, doi: 10.1029/2006GL026126.

Martin, S. T. 2000. Phase transitions of aqueous atmospheric particles. *Chem. Rev.* **100**, 3403–3453.

Matsuki, A., Schwarzenboeck, A., Venzac, H., Laj, P., Crumeyrolle, S. and co-authors. 2010. Cloud processing of mineral dust: direct comparison of cloud residual and clear sky particles during AMMA aircraft campaign in summer 2006. *Atmos. Chem. Phys.* **10**, 1057–1069.

Min, Q.-L., Li, R., Lin, B., Joseph, E., Wang, S. and co-authors. 2009. Evidence of mineral dust altering cloud microphysics and precipitation. *Atmos. Chem. Phys.* **9**, 3223–3231.

Moreno, T., Querol, X., Castillo, S., Alastuey, A., Cuevas, E. and co-authors. 2006. Geochemical variations in aeolian mineral particles from the Sahara–Sahel Dust Corridor. *Chemosphere* **65**, 261–270.

Müller, T., Schladitz, A. and Wiedensohler, A. 2011. Spectral particle absorption coefficients, single scattering albedos, and imaginary parts of refractive indices from ground based in-situ measurements at Cape Verde Island during SAMUM-2 *Tellus* **63B**, this issue.

Nousiainen, T. 2009. Optical modeling of mineral dust particles: a review. *J. Quant. Spectrosc. Ra.* **110**, 1261–1279.

Okada, K., Heintzenberg, J., Kai, K. and Qin, Y. 2001. Shape of atmospheric mineral particles collected in three Chinese arid-regions. *Geophys. Res. Lett.* **28**, 3123–3126.

Ouimette, J. R. and Flagan, R. C. 1982. The extinction coefficient of multicomponent aerosols. *Atmos. Environ.* **16**, 2405–2419.

Palik, E. D. 1985. Potassium chloride (KCl). In: *Handbook of Optical Constants of Solids I* (ed. Palik E.D.). Academic Press, San Diego, 703–718.

Petit, R. H., Legrand, M., Jankowiak, I., Molinié, J., Asselin and co-authors. 2005. Transport of Saharan dust over the Caribbean Islands: study of an event. *J. Geophys. Res.* **110**, D18S09, doi:10.1029/2004JD004748.

Philipp, H. R. 1985. Silicon dioxide (SiO_2), type α (Crystalline). In: *Handbook of Optical Constants of Solids I* (ed. Palik, E.D.). Academic Press, San Diego, 719–747.

Podczeck, F., Rahman, S. R. and Newton, J. M. 1999. Evaluation of a standardised procedure to assess the shape of pellets using image analysis. *Int. J. Pharm.* **192**, 123–138.

Rasband, W. S. 2010. ImageJ. U. S. National Institutes of Health, Bethesda, Maryland, USA. Available at: http://rsb.info.nih.gov/ij/. Accessed on 01-July-2010.

Redmond, H. E., Dial, K. D. and Thompson, J. E. 2010. Light scattering and absorption by wind blown dust: theory, measurement, and recent data. *Aeolian Res.* **2**, 5–26.

Reid, E. A., Reid, J. S., Meier, M. M., Dunlap, M. R., Cliff, S. S. and co-authors. 2003a. Characterization of African dust transported to Puerto Rico by individual particle and size segregated

bulk analysis. *J. Geophys. Res.* **108**, 8591, PRD 7-1-PRD 7-22, doi: 10.1029/2002JD002935.

Reid, J. S., Jonsson, H. H., Maring, H. B., Smirnov, A., Savoie, D. L. and co-authors. 2003b. Comparison of size and morphological measurements of coarse mode dust particles from Africa. *J. Geophys. Res.* **108**, 8593, PRD 9-1-PRD 9-28, doi: 10.1029/2002JD002485.

Ribarski, M. W. 1985. Titanium dioxide (TiO_2) (Rutile). In: *Handbook of Optical Constants of Solids I* (ed. Palik, E.D.). Academic Press, San Diego, 795–804.

Ro, C.-U., Osán, J., Szalóki, I., de Hoog, J., Worobiec, A. and co-authors. 2003. A Monte Carlo Program for quantitative electron-induced X-ray analysis of individual particles. *Anal. Chem.* **75**, 851–859.

Satheesh, S. K. and Krishna Moorthy, K. 2005. Radiative effects of natural aerosols: a review. *Atmos. Environ.* **39**, 2089–2110.

Scheuvens, D., Kandler, K., Küpper, M., Lieke, K., Zorn, S. and co-authors. 2011. Indiviual-particle analysis of airborne dust samples collected over Morocco in 2006 during SAMUM 1. *Tellus* **63B**, this issue.

Schkolnik, G., Chand, D., Hoffer, A., Andreae, M. O., Erlick, C. and co-authors. 2007. Constraining the density and complex refractive index of elemental and organic carbon in biomass burning aerosol using optical and chemical measurements. *Atmos. Environ.* **41**, 1107–1118.

Schladitz, A., Müller, T., Nowak, A., Kandler, K., Lieke, K. and co-authors. 2011. In situ aerosol characterization at Cape Verde. Part 1: Particle number size distributions, hygroscopic growth and state of mixing of the marine and Saharan dust aerosol. *Tellus* **63B**, this issue.

Schnaiter, M., Linke, C., Möhler, O., Naumann, K.-H., Saathoff, H. and co-authors. 2005. Absorption amplification of black carbon internally mixed with secondary organic aerosol. *J. Geophys. Res.* **110**, 1–11, D19204, doi: 10.1029/2005JD006046.

Shinn, E. A., Smith, G. W., Prospero, J. M., Betzer, P., Hayes, M. L. and co-authors. 2000. African dust and the demise of Caribbean coral reefs. *Geophys. Res. Lett.* **28**, 3029–3032.

Sokolik, I. N. and Toon, O. B. 1999. Incorporation of mineralogical composition into models of the radiative properties of mineral aerosol from UV to IR wavelengths. *J. Geophys. Res.* **104**, 9423–9444.

Sullivan, R. C., Guazzotti, S. A., Sodeman, D. A., Tang, Y., Carmichael, G. R. and co-authors. 2007. Mineral dust is a sink for chlorine in the marine boundary layer. *Atmos. Environ.* **41**, 7166–7179.

Sullivan, R. C., Moore, M. J. K., Petters, M. D., Kreidenweis, S. M., Roberts, G. C. and co-authors. 2009. Effect of chemical mixing state on the hygroscopicity and cloud nucleation properties of calcium mineral dust particles. *Atmos. Chem. Phys.* **9**, 3303–3316.

Swap, R., Garstang, M., Greco, S., Talbot, R. and Kållberg, P. 1992. Saharan dust in the Amazon Basin. *Tellus* **44B**, 133–149.

Tang, I. N. 1996. Chemical and size effects of hygroscopic aerosols on light scattering coefficients. *J. Geophys. Res.* **101**, 19245–19250.

Tegen, I. 2003. Modeling the mineral dust aerosol cycle in the climate system. *Quarter. Sci. Rev.* **22**, 1821–1834.

Tropf, W. J. 1998. Calcium carbonate, calcite ($CaCO_3$). In: *Handbook of Optical Constants of Solids III* (ed. Palik, E.D.). Academic Press, San Diego, 701–715.

Twohy, C. H., Kreidenweis, S. M., Eidhammer, T., Browell, E. V., Heymsfield, A. J. and co-authors. 2009. Saharan dust particles nucleate droplets in eastern Atlantic clouds. *Geophys. Res. Lett.* **36**, 1–6, L01807, doi: 10.1029/2008gl035846.

Ullerstam, M., Vogt, R., Langer, S. and Ljungström, E. 2002. Thi kinetics and mechanism of SO_2 oxidation by O_3 on mineral dust. *Phys. Chem. Chem. Phys.* **4**, 4694–4699.

Usher, C. R., Al-Hosney, H., Carlos-Cuellar, S. and Grassian, V. H. 2002. A laboratory study of the heterogeneous uptake and oxidation of sulfur dioxide on mineral dust particles. *J. Geophys. Res.* **107**, 4713, ACH 16-1-ACH 16-9, doi: 10.1029/2002JD002051.

VDI 1997. *Measurement of Particulate Precipitations – Microscopic differentiation and size fractionated determination of particle deposition on adhesive collection plates – Sigma-2 sampler*. Guideline 2119, Sheet 4. Berlin, Beuth Verlag.

Worringen, A., Ebert, M., Trautmann, T., Weinbruch, S. and Helas, G. 2008. Optical properties of internally mixed ammonium sulfate and soot particles—a study of individual aerosol particles and ambient aerosol populations. *Appl. Optics* **47**, 3835–3845.

Zhang, D., Iwasaka, Y., Matsuki, A., Ueno, K. and Matsuzaki, T. 2006. Coarse and accumulation mode particles associated with Asian dust in southwestern Japan. *Atmos. Environ.* **40**, 1205–1215.

Zimmermann, F., Weinbruch, S., Schütz, L., Hofmann, H., Ebert, M. and co-authors. 2008. Ice nucleation properties of the most abundant mineral dust phases. *J. Geophys. Res.* **113**, 1–11, D23204, doi: 10.1029/2008JD010655.

Supporting Information

Additional supporting information may be found in the online version of this article:

Appendix S1
Table S1

Please note: Wiley-Blackwell is not responsible for the content or functionality of any supporting materials supplied by the authors. Any queries (other than missing material) should be directed to the corresponding author for the article.